

Special Issue

Physical Characterization of Thin-film Solar Cells

Ken Durose^{1,*†}, Sally E. Asher², Wolfram Jaegermann³, Dean Levi², Brian E. McCandless⁴, Wyatt Metzger², Helio Moutinho², P.D. Paulson⁴, Craig L Perkins², James R. Sites⁵, Glenn Teeter² and Mathias Terheggen⁶

¹Department of Physics, University of Durham, South Road, Durham DH1 3LE, UK

²National Renewable Energy Laboratory, 1617 Cole Blvd. MS 3215, Golden, CO 80401-3393, USA

³Institute of Materials Science, Darmstadt University of Technology, Darmstadt, Germany

⁴Institute for Energy Conversion, University of Delaware, Newark, DE 19716, USA

⁵Physics Department, Colorado State University, Fort Collins, CO 80525, USA

⁶ETH Zürich, Institut für Angewandte Physik, CH-8093, Zürich, Switzerland

The principal techniques used in the physical characterization of thin-film solar cells and materials are reviewed, these being scanning probe microscopy (SPM), X-ray diffraction (XRD), spectroscopic ellipsometry, transmission electron microscopy (TEM), Auger electron spectroscopy (AES), secondary-ion mass spectrometry (SIMS), X-ray photoelectron spectroscopy (XPS), photoluminescence and time-resolved photoluminescence (TRPL), electron-beam-induced current (EBIC) and light-beam-induced current (LBIC). For each method the particular applicability to thin-film solar cells is highlighted. Examples of the use of each are given, these being drawn from the chalcopyrite, CdTe, Si and III–V materials systems. Copyright © 2004 John Wiley & Sons, Ltd.

KEY WORDS: thin-film solar cell; characterization; chemical analysis; microstructure; optical properties; spatially resolved functionality

ABBREVIATIONS: AES, Auger electron spectroscopy; AFM, atomic force microscopy; CBD, chemical bath deposition; CIGS, copper indium gallium diselenide; CSS, close-spaced sublimation; EBIC, electron-beam-induced current; EDS, energy-dispersive X-ray spectroscopy; EELS, electron-energy loss spectroscopy; EMA, effective medium approximation; FIB, focused-ion-beam; GIXRD, glancing-incidence X-ray diffraction; HRTEM, high-resolution transmission electron microscopy; ITO, indium tin oxide; KPFM, Kelvin probe force microscopy; LBIC, laser-beam-induced current; PL, photoluminescence; PMT, photomultiplier tube; PV, photovoltaic; PVD, physical-vapour deposition; QE, quantum efficiency; RTSE, real-time spectroscopic ellipsometer; SAM, scanning Auger microscope; SCM, scanning capacitance microscopy; SEM, scanning electron microscope; SIMS, secondary ion mass spectrometry; SPM, scanning probe microscopy; STM, scanning tunnelling microscopy; STS, scanning tunnelling spectroscopy; TCO, transparent conducting oxide; TEM, transmission electron microscopy; TRPL, time-resolved photoluminescence; XES, X-ray emission spectroscopy; XPS, X-ray photoelectron spectroscopy; XRD, X-ray diffraction.

INTRODUCTION

The requirements for thin-film semiconductor solar cell device structures are simple in comparison to most routinely produced electronic and optoelectronic structures: there should be a strong optical absorber; this must be coupled with a window layer to constitute a heterojunction; an electrical junction should be engineered within it to effect collection; ohmic contacts should be applied. The optimum materials

*Correspondence to: Ken Durose, Department of Physics, University of Durham, South Road, Durham DH1 3LE, UK.

†E-mail: ken.durose@durham.ac.uk

Contract/grant sponsor: US National Renewable Energy Laboratory.

Contract/grant sponsor: US Department of Energy; contract/grant number: DE-AC36-99GO10337.

choices are well known. Nevertheless the development of a viable thin-film technology has been fraught with difficulties, some fundamental, others originating from empiricism during the drive to demonstrate high-efficiency devices. Three well-known confounding factors are that:

- (a) Grain boundaries influence recombination, current transport and diffusion/segregation. The outcomes of influencing grain boundaries by growth, processing and ageing need to be measured in terms of device response and local device behaviour—but ultimately understood in terms of (for example) local charge states and chemical profiles;
- (b) Fundamental hurdles such as the electron affinity of absorbers make contacting an issue for some materials systems. Considerable technological effort has been deployed, but this is most effective when underpinned by understanding issues such as band line-ups in conjunction with device theory;
- (c) Point defects in thin-film solar cells are not understood. In conventional semiconductor processing the conductivity and field profile of a device is engineered by controlled doping with well-understood centres. In thin-film solar cell processing this is achieved empirically, without knowledge of the identity of the active centres, without knowing important sources of compensating species and even at the expense of sacrificing stability.

Clearly no single experimental diagnostic approach is capable of yielding all the diverse information relevant to the development of thin-film solar cells. The package of physical techniques used in the field can appear arbitrary—unless the specificity of each is understood and the picture generated by the whole appreciated. Moreover the results of physical techniques alone should not be taken in isolation from bulk photovoltaic (PV) response measurement, growth/processing conditions, nor even from device history.

Here some of the important physical characterization techniques for semiconductors are reviewed from the perspective of thin-film solar cells. The applicability of each to thin-film solar cells will be outlined and the reader will be referred to standard sources for further details of the principles of operation and applications. Examples of the output of each type of investigation are given from a range of solar cell materials systems: the intention is to provide an indication of the strengths of each method for thin-film PV rather than to generate a comprehensive treatise on any given material.

The sections for each technique that follow are ordered so as to progress broadly from measuring the physical outcomes of growth and processing, through basic materials parameters that determine (or else indicate) functionality, and ending with those techniques that reveal spatially resolved functionality at a materials and device level. These distinctions are blurred, and are perhaps arbitrary. Certainly all of the methods reviewed here contribute actively in the cycle of design, growth, processing, measurement, understanding and feedback in the development of viable devices. It is these capabilities that unify this portfolio of techniques.

SCANNING PROBE MICROSCOPY (SPM)

SPM^{1,2} is a general name for a group of techniques that utilize a very sharp probe, scanning over the sample surface. The type of interaction between the probe and the material defines the kind of SPM. Because the probe-sample interaction depends on the size of the tip, the shape of the surface, and the kind of interaction, the lateral resolution of these techniques varies from about 1 Å to several hundred angstroms. The first SPM technique was scanning tunnelling microscopy (STM),^{3,4} developed by Heinrich Rohrer and Gerd Binnig in 1981. For their invention, they were awarded the Nobel Prize for Physics in 1986. STM consists of scanning a very sharp metallic tip (in general Mo or Pt/Ir alloy) a few angstroms above the sample surface, while applying an electric potential between them. A tunnelling current is established, which is exponentially dependent on the tip-sample separation, besides other parameters. An image of the surface is generated by scanning the tip laterally, and measuring the variation of the current (current image) or by using a feedback loop, which keeps the current constant by moving the tip closer to or away from the surface (topographic image), as the current tries to decrease or increase, respectively, due to changes in surface topography. These two kinds of image are common to almost all SPM techniques; one is generated by measuring the variation of the interaction, the other by keeping the magnitude of the interaction constant by moving the tip up or down. The high sensitivity of the tunnelling current with small variations of tip-sample separation allows STM to provide atomic images of

atomically flat surfaces. Nevertheless, in general, atomic imaging requires a pristine surface and the use of ultra-high vacuum. Because a current has to be established between the tip and the sample, only metals and semiconductors can be analysed by STM. There are also other modes in STM, called scanning tunnelling spectroscopy (STS), where information on the electronic structure of the surface can be obtained. The variation in tunnelling current with applied voltage gives rise to $I \times V$ and $dI/dV \times V$ measurements, which are examples of STS.

The second SPM technique was atomic force microscopy (AFM),^{5,6} which uses the force between the tip and the surface to generate the image. In the common set-up, a laser beam is reflected off the top of a cantilever, which carries the tip, and focused on two photodiodes mounted side by side. During scanning the tip, and consequently the cantilever, goes up and down, and the laser beam moves towards one detector or the other, generating an error signal. The error signal can be monitored, generating an error image, or a piezo can adjust the vertical position of the tip (or sample), to keep the error signal equal to zero. In this case, the voltage applied to the piezo is monitored, generating a topographic image. System calibration is achieved by imaging standard samples having known dimensions. There are three basic modes of AFM: contact, non-contact and intermittent contact, also known as tapping mode (name patented by Digital Instruments). In contact mode, the tip touches the surface while scanning laterally. The force between tip and sample is repulsive, and set by the controlling software. In the other modes, the tip oscillates several angstroms above the surface while scanning laterally, and the interaction is attractive. Even in non-contact mode the tip may end up contacting the surface if the water layer, generally present on the sample surface in air, is thicker than the tip-sample separation. Although STM is more convenient for atomic imaging, AFM has the advantage of being able to analyse almost any type of sample, including insulators. Furthermore it is generally much easier to acquire images in AFM than in STM mode. Images of the surface of thin films can be obtained with up to atomic resolution, although this requires an atomically flat film. In many cases, the resolution is limited to a few dozen angstroms. The collected data, in standard AFM and STM analysis, are the vertical position z of the tip at each lateral position x, y , giving rise to a matrix. When these data are shown on a drawing program, it looks like the topography of the sample, similar to a scanning electron microscope (SEM) micrograph. Nevertheless, SPM provides digital data, as opposed to a picture, and, for this reason, the technique can provide real three-dimensional images and quantitative measurements, such as angle between features and roughness, which are important properties of thin films used in PV applications. It is important to realize that both AFM and STM images are obtained by a convolution between the tip and sample images. So, tip artifacts are inherent to SPM images, and the goal is to have a long narrow tip with a very small radius, to minimize these artifacts. Commercial tips have radii varying from 2 to 200 nm, depending on the SPM mode.

Based mainly on the AFM, several new techniques have been developed in recent years. In this paragraph, we will briefly describe some of these techniques. Lateral force microscopy^{7,8} uses a detector divided into four quadrants, and monitors the twist of the cantilever as it scans the surface. Regions where the friction between the tip and the cantilever is higher will twist the cantilever more, and produce a higher contrast in the image. Measurements of hardness can be done by using a hard tip, pressing it into the surface, and measuring the cantilever deflection versus the vertical movement of the piezoelectric drive. Electrostatic force microscopy^{9,10} uses a voltage between the tip and the sample to measure changes in the electrical properties of the sample surface. By using a feedback circuit to control the DC voltage, quantitative measurements of surface potential can be obtained; this technique is called Kelvin probe force microscopy (KPFM).¹¹ Scanning capacitance microscopy (SCM)¹² measures the capacitance between the probe and the surface, and the signal is proportional to the density of carriers in the semiconductor. With suitable models, quantitative measurements of the carrier concentration can be obtained with this technique.¹³ All of the above modes are more or less influenced by the topography of the sample, and care is needed to recognize topographic features on the acquired data. Also, although many of these measurements can be done by other methods, none of them can provide the spatial resolution obtained with SPM. Owing to their nature, AFM-based techniques are applied to the research of photovoltaic material more widely than STM. STM is more convenient when atomic resolution is needed, but this demands atomically flat surfaces that are not usually available with photovoltaic materials. An example of the use of STM to study PV materials is the investigation of arsenic-exposed Ge surfaces,¹⁴ to gain more insight into the nucleation of GaAs on Ge. Recently, there has been a significant increase in the use of SPM techniques to study the electrical properties of photovoltaic materials and devices. For instance, KPFM has been used to study the CuGaSe₂ surface,¹⁵ Mo/CuGaSe₂/CdS/ZnO devices,¹⁶ and GaInP₂ solar cells.¹⁷ SCM has

been used to study single grains and grain boundaries in CdTe,¹⁸ and AFM, measuring local electric current, has been used to study hydrogenated microcrystalline silicon.¹⁹ Below, we describe two examples of the use of standard AFM to study CdTe and CdS thin films used in solar cells.

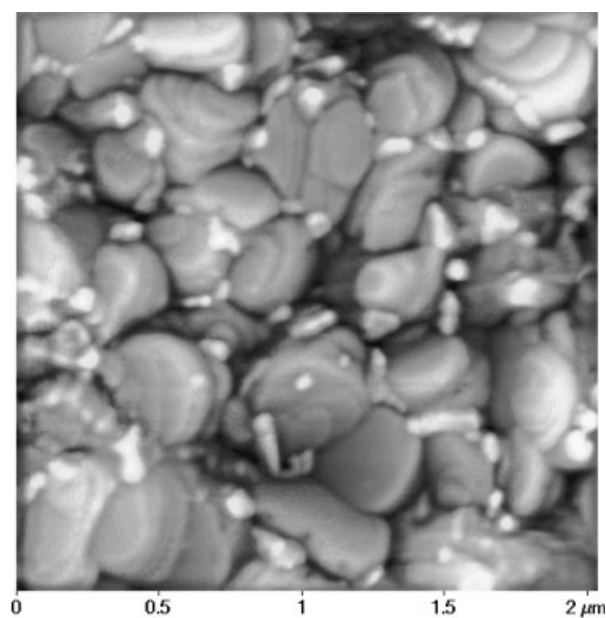
The first case is a study of recrystallization of CdTe thin films during heat treatment with CdCl₂/methanol solution.^{20–22} AFM was used to study the morphology of the thin films grown by different methods, before and after treatment. It was possible to observe the initial stages of the recrystallization of physical vapour deposition (PVD) films treated at 350°C for 30 min (Figure 1a) and the complete recrystallized films after the treatment at 400°C for 30 min (Figure 1b). In Figure 1(a), the large grains belong to the original CdTe film, while the small grains were formed by parts of the original structure that started to recrystallize as a means to decrease the large stress in the film. Increasing the treatment temperature accelerates the process, and the recrystallization process is completely finished after 30 min, as shown in Figure 1(b). In this case, the small grains seen in Figure 1(a) have consumed the whole original structure (large grains), and the sample is completely recrystallized. It was also shown that CdTe grown by close-spaced sublimation (CSS) did not recrystallize, because the amount of stress in these films was much smaller than in PVD films. Nevertheless, for films grown by CSS at temperatures almost 200°C lower than in the standard process, recrystallization during CdCl₂ treatment *did* occur. In the second example, CdS films were deposited by CSS and chemical bath deposition (CBD), in order to investigate why the best PV devices were obtained using CBD CdS.²³ It was found that one of the reasons for the best performance of the CBD CdS was that, unlike the CSS CdS, these films grew conformally on the underlying SnO₂ film, which was used as a front contact. The conformal growth promotes a film with a more uniform thickness, minimizing shunting paths. Figure 2 shows an AFM image of a CBD CdS film grown on SnO₂. The small grains are the CdS, while the big bumps are due to the underlying SnO₂, showing very good conformal coverage. Roughness measurements show that, although the morphology of the CdS and SnO₂ films are very different, their roughness is practically the same, which is due to the conformal growth.

X-RAY DIFFRACTION (XRD)

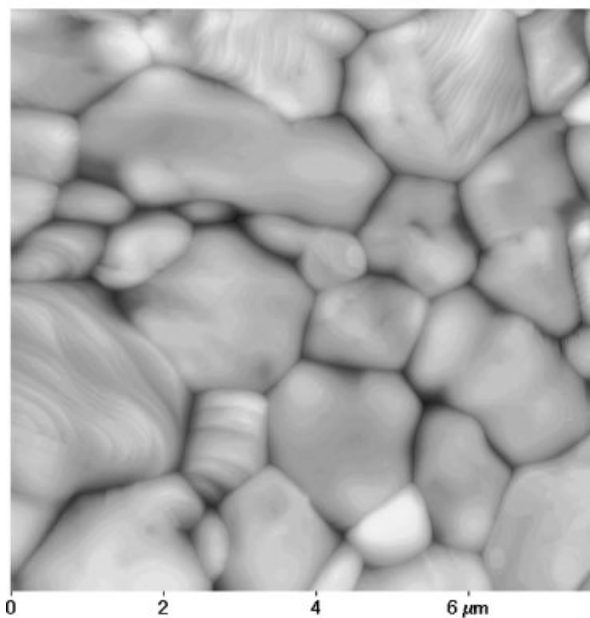
XRD is a powerful non-destructive analysis tool that provides quantitative information on the crystalline phases in thin films and thin-film structures. With a suitable choice of X-ray source and optical geometry, XRD analysis can be applied to a wide range of polycrystalline and microcrystalline materials used for PV. When used in conjunction with chemical analyses, a detailed description of thin-film structures can be developed. XRD methods are based on the scattering of X-rays by the atoms in a periodic array, i.e., the lattice. Coherent scattering occurs when the phase difference between the scattered waves from atoms in the lattice planes is a multiple of 2π , a condition that is geometrically met when the path length difference of the scattered waves is an integral number of wavelengths λ . The trick is locating the specimen and detector at positions in space with respect to the incident beam so that diffraction maxima can be detected. Different schemes, such as the rotating crystal method, the Laue method and the powder method are widely used for crystallographic analysis.²⁴ For thin films, variations of the powder method are utilized, having a powder or film specimen lying tangentially to a focusing circle defined by the distance between the X-ray source emergent slit and the specimen. In this method, an intensity maximum in the diffracted wavefront is found when the angular relationship between the incident and diffracted beams θ_i and θ_d for a given lattice plane spacing d_{hkl} corresponding to a particular crystallographic direction $\langle hkl \rangle$ is an integral number of wavelengths:

$$n\lambda = 2d_{hkl} \sin\left(\frac{\theta_i + \theta_d}{2}\right)$$

which is the Bragg equation. The diffraction intensity pattern for monochromatic X-rays as a function of the diffraction angle defined by $2\theta = \theta_i + \theta_d$ contains two primary pieces of information: (i) the overall pattern of diffracted peak positions represents the instrument-transform of the family of lattice plane spacings, which relates to the specific crystalline phases present; (ii) individual line profiles contain the instrument-transformed distribution of d -spacings at that crystallographic $\langle hkl \rangle$ direction, which in turn is related to compositional or structural distortions of the assemblage of atoms in that plane. Thus, XRD analysis consists of decoupling



(a)



(b)

Figure 1. AFM images of PVD CdTe thin films after CdCl_2 /methanol treatment then annealing for 30 min at (a) 350°C; and (b) 400°C. The large grains in (a) are recrystallized while the small ones are remnants of the as-grown structure. In (b) the higher annealing temperature has promoted more complete recrystallization

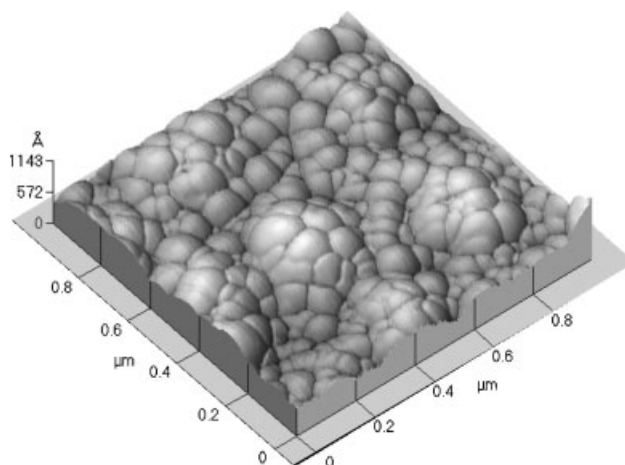


Figure 2. AFM image of a CBD CdS film grown on SnO₂. The small-scale granular structure represents individual CdS grains while the larger-scale ($\sim 0.4 \mu\text{m}$) undulations are the same as seen on the underlying SnO₂. Conformal growth, and the high uniformity of the film thickness, are considered to reduce shunting paths in finished devices

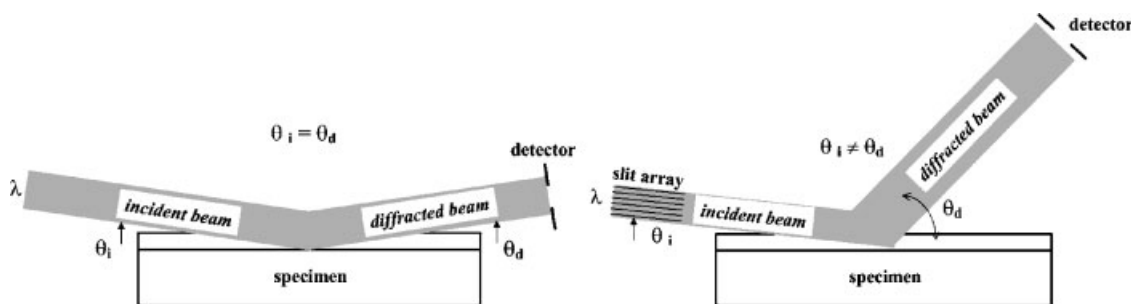


Figure 3. Symmetric and asymmetric thin-film XRD measurement configurations

instrumental effects (geometry and optical aberrations) from specimen-related effects (phases, and properties thereof).

Two optical configurations that are routinely applied for thin-film XRD analysis derive from parafofocusing cameras: *symmetric* Bragg-Brentano geometry²⁴ and *asymmetric* Seeman-Bohlin geometry^{25,26} (Figure 3). In either optical configuration, the X-ray source intensity and angular dispersion are fixed by the take-off angle from the X-ray source to the entrance slit. The angular intensity distribution $h(2\theta_d)$ obtained on the detector arc represents the convolution of the optical transformation function (instrument function) $g(2\theta)$ with the specimen lattice distortion function, $f(2\theta)$:²⁷

$$h(2\theta) = \int_{-\infty}^{+\infty} g(2\theta)f(2\theta - \delta)d\delta$$

Instrumental effects in powder diffraction are described in detail in the literature.²⁷

The symmetric condition, $\theta_i = \theta_d$, constrains the measurement to lattice planes parallel to the specimen plane, and the specimen is equidistant from source and detector. The asymmetric condition, with $\theta_i \neq \theta_d$ and using fixed-incident beam angle, constrains the measurement to populations of lattice planes that are tilted with respect to the specimen plane. Asymmetric measurements made with low incident beam angles are referred to as glancing-incidence X-ray diffraction (GIXRD). In either symmetric or asymmetric diffraction, the minimum angle for diffraction from a specular specimen is governed by the critical angle θ_c , for total external reflection,²⁸ which for Cu K α radiation is $\theta_c \sim 0.2^\circ$ for Si and $\theta_c \sim 0.3^\circ$ for CdTe and CuInSe₂. A more complete analysis of the evanescent and reflected waves allows quantitative properties of multilayer thin-film stacks to be

Table I. Mass absorption coefficient (μ/ρ) and sampling depth (τ) for 1° incident beam angle and different x-ray sources for thin-film photovoltaic absorber layer materials

	CdTe	CuInSe ₂	α -Si
Mo K α (0.017 MeV)			
μ/ρ (cm ² /g)	35	69	8
τ (μ m) @ $\theta_i = 1^\circ$	0.85	0.44	11.5
Cu K α (0.008 MeV)			
μ/ρ (cm ² /g)	260	130	50
τ (μ m) @ $\theta_i = 1^\circ$	0.12	0.23	1.8
Cr K α (0.0054 MeV)			
μ/ρ (cm ² /g)	820	385	210

determined from glancing-incidence diffraction measurements.²⁹ The symmetric geometry is the most commonly encountered configuration in commercially available XRD powder diffraction systems. In older systems, the incident beam and X-ray source were mechanically fixed, the sample rotated through θ , and the detector rotated through 2θ by means of a geared goniometer. Present-day systems employ independent optically encoded goniometer arms to move the source and detector, while the specimen remains fixed. In either case, the symmetric configuration ensures that the diffraction condition will be met only for lattice planes that are tangential to the focusing circle, i.e., parallel to the plane of the specimen surface or holder. The mass absorption coefficient μ/ρ , which depends on the X-ray energy and chemical composition of the phase, causes low-index $\{hkl\}$ planes (large d -spacing, low 2θ) to be diffracted from near the powder surface, while high-index planes (low d -spacing, high 2θ) diffract from deeper into the powder. Table I lists mass absorption coefficients and sampling depths for different thin-film PV absorber layers and Mo, Cu and Cr radiation.

Quantitative powder diffraction analysis relies on homogeneous distribution and random orientation of the particulates, so that the diffracted intensity distribution received at the detector is governed only by the pure scattering properties of each $\{hkl\}$ reflection of each phase, and by the diffractometer instrument function. The detection limit of a trace phase in a majority phase matrix depends on the scattering properties of the phases; for similarly scattering phases, the detection limit for powder diffraction is ~ 0.5 wt%.

The quantities commonly sought from thin-film diffraction are phase identification, texture coefficient (orientation), lattice parameter, coherency length and volume fraction. Phases are identified by comparison of d -spacing and intensity rank of the peaks to published standards (at the International Centre for Diffraction Data, Newtown Square, PA, USA; formerly Joint Committee for Powder Diffraction Standards). The degree of preferred orientation P_{hkl} is calculated from peak intensities of wide-angle scans using the method of Harris for polycrystalline fibre texture analysis:³⁰

$$P_{hkl} = N \left(\frac{I_{hkl}}{I_{hkl}^0} \right) \left(\sum_{hkl=1}^N \frac{I_{hkl}}{I_{hkl}^0} \right)^{-1}$$

where N is the number of peaks in the angular range considered, I_{hkl} is the measured intensity of peak (hkl), and I_{hkl}^0 is the relative intensity of the corresponding peak from a random powder standard. For $P_{hkl} = N$, all the grains of the films are oriented in the $\langle hkl \rangle$ direction normal to the specimen plane, while $P_{hkl} = 1$ indicates random grain orientation and $P_{hkl} < 1$ indicates a preferred orientation along an axis other than $\langle hkl \rangle$. Precision lattice parameter is determined by reduction of d -spacings to lattice parameter, followed by removal of the effects of instrumental distortion and systematic error using an appropriate function, such as that found by Nelson and Riley³¹ and Sinclair and Taylor.³² Coherency length L , the average dimension of material volume producing coherent diffraction, influences the pure diffraction line width B , and is estimated using the Scherrer equation, assuming spherical particle shape:³³

$$L = \frac{0.94\lambda}{B \cos \theta}$$

where θ is the Bragg angle. The value B is properly obtained from experimental data by Fourier deconvolution of the instrument function from the measured line profile of a particular $\{hkl\}$ line for the phase in question.

Otherwise, if a single-mode gaussian distribution is assumed, an estimate can be obtained using $B^2 = W_S^2 - W_I^2$, where W_S and W_I are the full-width at half maximum of the specimen and the instrument, respectively. In thin films, low values of coherency length can be due to grain size or crystallographic defects, such as twinning. For Cu K α radiation, coherency lengths less than ~ 200 nm result in detectable peak broadening. In cases where a distribution of coherency lengths is suspected, a rigorous analysis of the line width variance³⁴ and line profile shape³⁵ is required. For many powder diffractometers adapted to thin-film analysis, the intensity distribution of the line profile $I(2\theta)$ is well-represented by the Pearson VII function:

$$I(2\theta) = I_b + I_0 \left[1 + \left(\frac{2(2\theta - 2\theta_c) \sqrt{2^{(1/m) - 1}}}{W_S} \right)^2 \right]^{-m}$$

where I_b is the background intensity, I_0 is the maximum intensity at the peak centrum $2\theta_c$, and m is the shape parameter. For $m = \infty$, the function resembles a gaussian distribution, and as m approaches 1, the function resembles a lorentzian distribution. At low values of 2θ , where axial divergence causes appreciable peak asymmetry, the split Pearson function is more applicable.³⁶

The phase volume fraction in mixtures can be determined from the relative peak intensity of the different phases, and the greatest accuracy is obtained for phases with random orientation. In the past, quantitative methods using individual peak intensities and mass absorption coefficients (for binary mixtures) or internal standards (for multi-phase mixtures) were used.³⁷ Today, whole-pattern fitting is routine, using Rietveld analysis, in which calculation of the instrument function, orientation distribution function and pure phase structure factors for all (hkl) lines of each phase are combined to model the measured powder diffraction pattern.^{36,38}

Other specimen-related properties such as intermixing and nonuniform strain can complicate the unique determination from symmetric uniaxial XRD measurements of thin films. Asymmetric GIXRD measurement at different incident beam angles allows surface phases to be separated from bulk phases³⁹ and can reveal the distribution of residual stress.⁴⁰ Use of the eulerian cradle, in which the relationship of the specimen to the incident beam can be varied through multiple axes, permits accurate determination of preferred orientation (pole figure) and strain. Methods for analysing measured strain in thin films to obtain the elastic constants are described in detail elsewhere.^{41,42}

Following are selected examples of applications of XRD and GIXRD techniques in thin-film PV research. In silicon-based thin-film devices, microcrystalline silicon films are under investigation for greater flexibility in device design and to improve stability. Figure 4 is a diffraction pattern of the (111) peak of two microcrystalline (μ -c) Si thin films, deposited by hot-wire chemical vapour deposition (HWCVD) at 430°C at different growth rates to a total thickness of 2 μ m. Both films are crystalline, and reduction using the Pearson VII distribution shows that the sample deposited at 1 μ m/h has more than twice the coherency length compared with the sample deposited at 5 μ m/h. Fabrication of PV devices from compound semiconductors and their alloys constitutes a significant branch of thin-film PV research. In particular, materials based on groups II–VI (e.g., CdTe, CdS, ZnTe) and I–III–VI (e.g., CuInSe₂, CuInS₂, CuGaSe₂) have received much attention. From a device perspective,

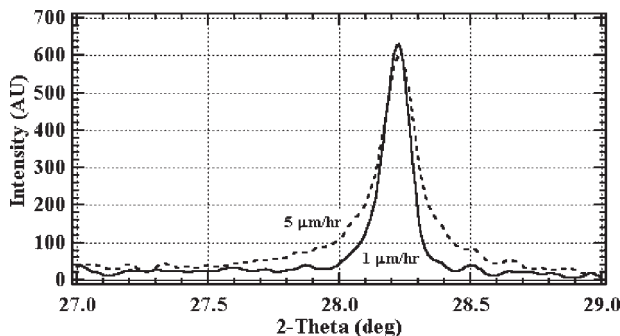


Figure 4. XRD of (111) region of silicon; thin-film deposited by hot-wire chemical vapour deposition (HWCVD) at $T = 430^\circ\text{C}$, for the deposition rates shown. For 1 $\mu\text{m/h}$, $W_S = 0.116^\circ$, $m = 2.5$ and $L = 102$ nm and for 5 $\mu\text{m/h}$ $W_S = 0.158^\circ$, $m = 1.0$ and $L = 41$ nm. The more slowly grown film has greater structural coherence

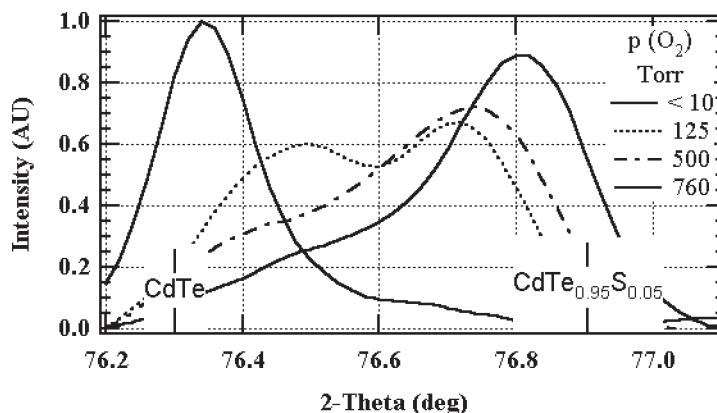


Figure 5. XRD of (511)/(333) region of zincblende CdTe and Cd(Te,S) alloy for CdTe/CdS films treated at 400°C for 20 min in $\text{CdCl}_2 + \text{O}_2 + \text{Ar}$ ambient at the O_2 partial pressures shown. The bimodal distribution for 125, 500 and 760 Torr O_2 arises from bimodal grain-size distribution in the CdTe film

the use of materials systems that readily form alloys offers control of structural and electronic properties such as lattice parameter, optical bandgap and band offsets. In processing CdTe/CdS thin-film structures, intermixing between the CdTe and CdS layers and oxidation of the CdTe surface can occur, which can have a significant impact on device operation.⁴³ Figure 5 shows the evolution of the CdTe (511)/(333) line profile for thin-film CdTe/CdS structures treated at 400°C for 20 min in vapour at 1 atm containing 9 mTorr CdCl_2 and different partial pressures of O_2 , with argon balance. The lattice parameter distribution evolves from nearly pure CdTe to the equilibrium alloy $\text{CdTe}_{0.95}\text{S}_{0.05}$ as $p(\text{O}_2)$ increases, showing a chemical dependence on the uptake of CdS by the CdTe film. Investigation of the dynamics of this process by modelling the diffusion process, accounting for actual grain size distribution, shows that grain boundary diffusion enhances the overall diffusivity of CdS in CdTe films,⁴⁴ and that both CdCl_2 and O_2 concentration in the treatment ambient can affect the grain boundary diffusion coefficient by over four orders of magnitude.⁴³ A similar XRD analysis was carried out on the conversion of CuInSe_2 to $\text{CuIn}(\text{Se}_{1-y}\text{S}_y)_2$ by reaction with sulfur-containing vapour.⁴⁵ During the process, S and Se exchanged via solid-state diffusion and solid-vapour reaction, reducing the lattice parameter. Analysis of primary recrystallization during CdCl_2 treatment of electrodeposited CdTe films showed Arrhenius behaviour for thermal activation of the change in texture coefficient, with an activation energy of 3.4 eV (B.E. McCandless, unpublished work). Thus, for CdTe/CdS devices, XRD analysis has shown how post-deposition processing affects both the internal properties of the individual CdTe and CdS films and the interaction between them.

Surface-sensitive diffraction methods such as GIXRD can reveal the crystalline properties of surfaces such as the thin contacts used for CdTe cells. Figure 6 shows wide-angle GIXRD scans of sequentially deposited 50-nm-thick Te, 30 nm Cu, and 50 nm Au films on borosilicate glass. The scan at $\theta_1 = 0.2^\circ$, near the critical angle for these materials, shows prominent Au peaks (Figure 6, *) and a weak peak of Cu_2Te (Figure 6, #) at $2\theta = 30^\circ$. At $\theta_1 = 0.5^\circ$, three additional Cu_2Te reflections are visible, as well as two peaks of Cu_3Te_2 (Figure 6, ×). At $\theta_1 = 1.0^\circ$, the Cu_3Te_2 reflections intensify, and elemental Te peaks (Figure 6, +) are visible. No elemental Cu or CuTe peaks are detected. This sequence shows that the terminating surface layer consists of Cu_2Te while the film at the Te surface consists of Cu_3Te_2 . Following brief annealing at 200°C, no elemental Te peaks were detected and the Cu_2Te peaks and Cu_3Te_2 peaks intensified. For relatively smooth films, models based on extinction and intensity factors can be used to quantitatively interpret GIXRD patterns for phase distribution. Finally, the asymmetric condition allows the stress tensor in the films to be determined by careful determination of peak positions for scans acquired at different incident angles.

SPECTROSCOPIC ELLIPSOMETRY

Employing visible light for thin-film metrology is a concept dating back to the 1830s. Interferometry and reflectometry techniques were considered as the basis for measuring minute thicknesses of transparent bodies

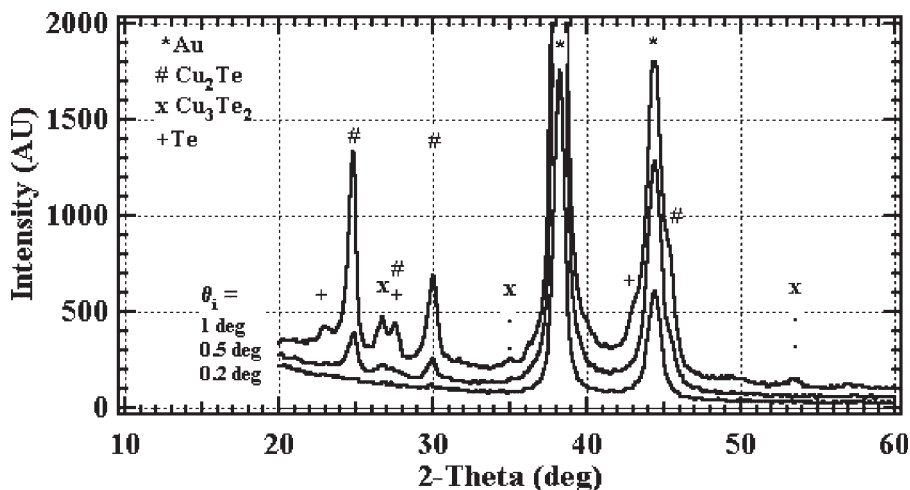


Figure 6. Wide-angle GIXRD scans of an Au(50 nm)/Cu(30 nm)/Te(50 nm) film stack taken at different incident-beam angles

by their colours.⁴⁶ In 1889 Drude added another dimension into the thin-film metrology by demonstrating thickness measurement using polarized light in 1889, which is now known as ellipsometry.⁴⁷ He utilized the difference between two mutually perpendicular polarized (*p*- and *s*-polarized) light beams to measure the thickness of thin films. Rothen introduced the name ellipsometry in 1945.⁴⁸ In early ellipsometers the human eye was the detector used to find the null point, and the repeatability of measurements was not good. The development of photomultiplier tubes (PMTs), lasers, fibre optics and fast computers has now greatly improved the repeatability, flexibility and speed of the ellipsometry measurement technique. It also facilitates the development of a wide variety of measurement configurations that are suitable for the different applications. Single-wavelength ellipsometry techniques are widely used in the microelectronic industries. With the development of microelectronics and sophisticated modelling software, the multichannel real-time spectroscopic ellipsometer (RTSE) has become increasingly popular in laboratories that characterize semiconductors. RTSE instruments are currently finding their way into the thin-film PV industry for *in situ* process control applications.

Ellipsometry measures the ratio of *p*- and *s*-complex reflectance of the sample; it differs from reflectometry, in which the ratio of intensity of the reflected beam to the incident beam is measured. This principle is clear from the fundamental equation governing ellipsometry:

$$\tan \Psi e^{i\Delta} = \frac{R^p}{R^s}$$

where R^p and R^s are the total complex reflection coefficients for *p*- and *s*-waves respectively. The parameter Ψ corresponds to the ratio of the magnitude of the total reflection coefficient and Δ is the phase shift in *p*- and *s*-waves due to the reflection. Ellipsometry measures Ψ and Δ , which together are known as the ellipsometry parameters, and useful information, i.e., thickness and optical constants, is extracted using optical models. Knowledge of the polarization state of the incident light as well as the reflected light is required for the determination of Ψ and Δ . Thus an ellipsometer consists of a light source, a polarizer to fix the polarization of the incident light, an analyser to measure the polarization state of the reflected light and a detector. With these basic components, the ellipsometer can be configured in a large number of modes; null, rotation analyser, rotation polarizer and polarization modulation. Figure 7 shows the basic ellipsometry configuration used for multilayer thin-film structure analysis.

Ellipsometry measurements can be performed as a function of wavelength (spectroscopic), incident angle (variable-angle single-wavelength/spectroscopic) and time (real-time/dynamic, single-wavelength/spectroscopic) depending on the requirements. An example is the determination of the thickness of the thermal

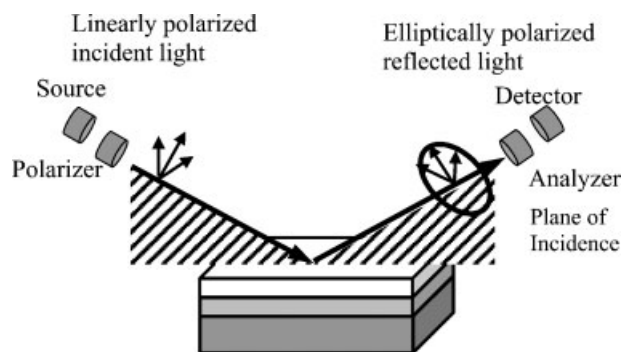


Figure 7. Typical ellipsometry measurement configuration used for a thin-film stack

oxide SiO_2 on Si. Since the optical constants of SiO_2 thermal oxide are invariant with the deposition condition and are isotropic one can use single-wavelength, single-incident-angle measurements to determine the thickness. However, spectroscopic measurements are required when examining materials for which the optical constants depend on the deposition conditions. Real-time measurements are suitable for process monitoring and control. A typical thin-film ellipsometry analysis consists of the following steps: (a) measurement of ellipsometry parameters Δ and Ψ ; (b) optical modelling to functionally describe the optical properties of the sample; (c) generation of data using the optical model; and (d) fitting model-generated data to minimize the error. The accuracy of the data obtained from an analysis depends primarily on the optical model. Several classical and quantum-mechanical oscillator models have been developed to describe the optical constants of material in a functional form. The most fundamental classical oscillator model is the Lorentz oscillator, which is equivalent to the classical mass on a spring. A Lorentz oscillator can be described using the relation

$$\varepsilon(h\nu) = \frac{A}{E^2 - (h\nu)^2 - iBh\nu}$$

where A is the amplitude, E is the centre energy, B is the broadening of the oscillator and $h\nu$ is the photon energy in eV.

Building an accurate optical model of a multilayer structure may require important information about the nature of the sample to be obtained, some of it dependent on the deposition conditions used. Non-ideal properties of the surface due to the presence of oxides or roughness are different from the bulk properties and must be incorporated in to the model accordingly. Since the spectroscopic ellipsometry technique uses specular light reflected from the sample surface to determine the sample properties, a significant amount of surface roughness can cause scattering, and hence affects the accuracy of the analysis. Surface roughness models employing the Bruggeman⁴⁹ effective medium approximation (EMA) require the surface roughness feature size to be less than 0.1λ , where λ is the wavelength of the probing light. This limitation applies equally to EMA models for homogeneous materials and those with voids.

The optical constants of thin-film PV materials are presently being extensively studied by spectroscopic ellipsometry in multilayer structures. For example, in Figure 8, ellipsometry analysis is used to determine the thickness and the optical constants of CdS film deposited on an ITO/glass substrate (where ITO is indium tin oxide). The optical model for the analysis is also shown along with optical constants of CdS and ITO obtained from the best fit. The ITO layer is modelled with two classical oscillators: a Lorentz oscillator to describe the electronic transition, and a Drude oscillator (Lorentz oscillator with zero energy) to describe the free carrier absorption. The CdS layer is modelled with two oscillators: a Lorentz oscillator to describe the optical transitions at higher energies, and gaussian broadened polynomial superposition (GBPS) semiconductor oscillators⁵² to describe the fundamental optical transitions. The optical model also consists of an intermixed layer and surface roughness layer, which are modelled with a Bruggemann⁴⁹ EMA. Depending on the deposition conditions, CdS films ideally grow in either wurtzite or zincblende structure. The wurtzite structure exhibits biaxial anisotropy

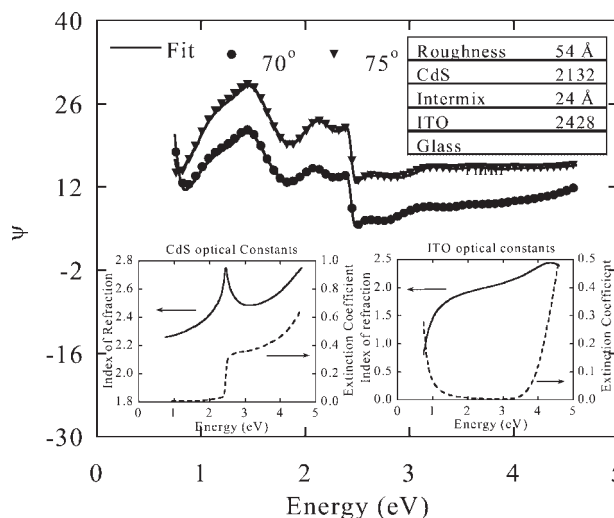


Figure 8. Measured and fitted ψ data for CdS/ITO/glass films at two different incident angles (70° and 75°) (The measured data are shown as points, the fits are shown as solid lines). The insets show the optical model and the optical constants obtained from the fit

and the optical properties of the CdS film therefore depend on the texture of the film (CdS displays ordinary optical constants along the c -axis and extraordinary ones perpendicular to it). The effective dielectric function of the polycrystalline material can be calculated as a tensorial average considering a medium composed of uniaxial crystals oriented in random directions.⁵³ If all the crystals have the same texture, the anisotropy of the polycrystalline material would be similar to the single crystal. However, if the polycrystalline material has the same probability of occurrence for all textures or is randomly structured, the optical properties of the material would be isotropic. The CdS film used for the above analysis is CdCl₂-treated, which makes the film randomly oriented. Hence the optical constants of CdS obtained from this analysis correspond to the ordinary component.

Semiconductor alloy models are employed to describe the changes in the optical constants of such materials as a function of alloy composition, and conversely to determine the alloy compositions from the optical constants.⁵⁴ Many of the PV thin-film properties change with thickness due to deposition conditions or post-deposition treatments. By incorporating several layers with gradually varying optical constants (for example a semiconductor alloy model with varying alloy fraction) into the analysis, one can also determine the compositional grading in the film. The evolution of structural changes due to the deposition conditions and the post-deposition treatments can therefore be studied effectively using ellipsometry. It can also be used to determine the effect of deposition and post-deposition treatments on the properties of an individual layer in a thin-film multilayer structure, making it a useful diagnostic tool for investigating device anomalies. For example, a change in the conductivity of the ITO as a result of change in the free carrier concentration can be modelled using the Drude oscillator model. The same idea can be used to analyse quantitatively the doping density in the semiconductor materials by performing ellipsometry measurements in the infrared region.⁵⁴ Furthermore, since the technique is highly sensitive to surface layers, it is readily used to analyse the effects of various back-contact etching processes on the semiconductor surfaces. The formation of an amorphous Te layer on CdTe followed by room-temperature crystallization as a result of nitric/phosphoric acid etching was studied using ellipsometry.⁵⁵

Spectroscopic ellipsometry measurements are useful in optimizing the Te thickness on CdTe by varying the etch solution concentration and etching time. Modulation ellipsometry was used to analyse the effect of light (photoellipsometry), magnetic field and thermal effect on the optical properties of the material. The photoellipsometry technique was employed to determine the built-in electric field strength at the surface and depletion width in AlGaAs/GaAs solar cells.⁵⁶

Ellipsometry measurements are predominantly suitable for routine non-destructive measurements on a known material system, where one is looking for deviations from the expected behaviour. This makes the

ellipsometry technique particularly ideal for process monitoring/control applications. For example, the structural evolution and optical properties of the various layers in *p-i-n* and *n-i-p* a-Si:H solar cells (hydrogenated amorphous silicon) were measured by multichannel RTSE.⁵⁷ New methods were developed to extract the thickness evolution of the $\mu\text{c-Si:H}$ volume fraction in mixed-phase amorphous and microcrystalline silicon [(a + μc)-Si:H] i-layers based on RTSE measurements performed during plasma-enhanced chemical vapour deposition of the films.⁵⁸ These analyses were critical for the optimization of a-Si:H-based solar cell fabrication.

TRANSMISSION ELECTRON MICROSCOPY (TEM)

Grain sizes in polycrystalline multilayer devices for PV applications vary from several hundred micrometres in polycrystalline Si (p:Si) to a few tens of nanometres in electrodeposited CdTe, and layer thicknesses are found to be in the same range from several hundred micrometres for absorber layers in p:Si to less than 20 nm for CdS buffer layers in Cu(In,Ga)Se₂ cells. In combination with grain boundary and interface-related phenomena such as grain boundary and surface charge-carrier recombination, segregation and interdiffusion, these scales define the resolution necessary for direct investigations in thin-film solar cells. TEM has been employed since the first studies on thin-film devices, because micrometre to sub-nanometre resolution is easily obtained with the high-energy electron probe used in TEM. Early applications of TEM were limited to structural investigations such as diffraction, diffraction contrast imaging^{59–62} and, later, high-resolution imaging of crystal lattices.^{63,64} But with the addition of electron-energy-loss spectroscopy (EELS) and energy-dispersive X-ray spectroscopy (EDS) among other analytical techniques, the so-called analytical TEM⁶⁰ has become indispensable for the structural and chemical characterization of polycrystalline multilayer films.

Sample preparation

The strong electron-specimen interaction requires the sample area to be less than 100 nm thick for TEM (less for high-resolution TEM, HRTEM) to ensure sufficient transmission of electrons. This makes sample preparation the crucial part of any TEM study. Moreover, the physical process of thinning a sample to electron transparency by mechanical, chemical and/or ion-beam means is a slow one that requires a good deal of operator skill. It cannot be emphasized enough that special care has to be taken to avoid the introduction of structural or chemical gradients during sample preparation. Many of the problems encountered during the subsequent microscopy studies, such as electrical charging of the sample, chemical smearing of interfaces or the presence of deformation defects, have to be planned for and avoided by careful sample preparation.

The two geometries appropriate to thin-film TEM studies are 'plan-view' and 'cross-section'. Plan-view studies are appropriate where a large area of a single layer in a stack is to be studied, for example where the grain size of buried layers is to be studied.⁶⁵ An example is given below. The preparation of electron-transparent foils for plan-view TEM can be complex and generally involves a combination of grinding, selective etching and ion-beam thinning.

For interface analysis, and to see the relationships between hetero-layers, cross-sectional sample preparation is required. As the layers used in thin-film devices are often of a heterogeneous nature, agents for uniform chemical etching are not available, and mechanical thinning followed by ion-beam milling is employed instead. Usually Ar⁺ ion thinning is used, but for II–VI and some In-containing semiconductors, Ar⁺ thinning results in the introduction of very high densities of stacking fault loops at the sample surfaces. Hence for CdTe and InP (for example), Ar⁺ thinning is used, but final thinning is done with I⁺ milling, which is damage-free. In recent years the Ga ion microscope has been developed and popularized as the focused-ion-beam (FIB) microscope, and has found a distinctive role in TEM specimen preparation. The instrument is essentially an SEM employing a liquid Ga ion-beam source for illumination. Adjusting the beam energy allows a transition from imaging to highly localized sputtering (milling). When making a TEM sample this allows a specific area to be selected and, by means of trenching, isolated as an electron-transparent sample. The thin section is either lifted from its host by a micro-manipulator or else is cut in a form that allows direct inspection in the microscope.

All aspects of TEM sample preparation are reviewed and updated in a regular conference series.^{66–68}

TEM: structural analysis

The principles of TEM, diffraction, imaging and analysis are fully explained in texts and reviews,^{59–62} especially that by Williams and Carter,⁶⁰ which is regarded as the standard text. In brief, the advantage of electron over light microscopy is primarily one of resolution: by using, for example, 100 keV electrons having a de Broglie wavelength of $\lambda = 0.0037$ nm rather than visible light ($\lambda \sim 500$ nm), there is a very significant reduction in the diffraction-limited resolution achievable, i.e.,

$$R = \frac{0.61\lambda}{n \sin \alpha}$$

where n is the refractive index and α the half-angle of acceptance of the imaging lens. Even though the diffraction limit is not achieved on account of electron lens aberrations, atomic-scale resolution can be achieved under appropriate imaging conditions. Diffraction phenomena are a key part of the principles of imaging, owing to the relationship between the diffraction conditions and the image type—and to the image contrast. Since the electron wavelengths are short, for inorganic crystals having interplanar spacings of 0.1–0.2 nm, the Bragg angle is typically $<1^\circ$. Hence all crystal planes that are approximately parallel to the electron beam satisfy the diffraction condition. The fact that many planes diffract simultaneously, and that there is a regular spot pattern characteristic of a given zone axis, is best understood with reference to the Ewald sphere construction for diffraction from a thin sample. The reader is referred elsewhere for details.⁶⁰ Diffraction methods are used in structural analysis of thin films, e.g., in determining the orientational relationships across grain boundaries and interfaces. In the case of thin-film polycrystalline materials there is the possibility of local variation of orientational relationships on a scale greater than that in the field of view of the TEM, and correlation with averaging methods such as XRD (e.g., texture analysis) is advisable. Diffraction information is also valuable for setting up imaging conditions and in interpreting contrast quantitatively. Local strain analysis and the determination of local lattice parameters can be achieved by analysis of diffraction patterns. While this can be achieved with conventional methods, there is a considerable improvement in precision available from the specialist techniques of convergent electron beam diffraction.⁶⁰

For the analysis of lattice defects, their density and spatial distribution, TEM imaging methods are required, the most common form being diffraction-contrast imaging as used in the so-called ‘conventional TEM’. As crystal defects support local tilts of the crystal lattice (e.g., near a dislocation), the proximity to the Bragg condition and hence the strength of the diffracted ray is changed locally. For the case where only one set of planes diffracts strongly, the contrast can be interpreted quantitatively. In particular, by imaging defects by using several specifically chosen Bragg reflections with non-parallel diffraction vectors g_{hkl} , the fault vectors that characterize defects can be evaluated. (After tilting to enhance diffraction by a particular set of planes, the beam is selected by means of an objective aperture.) The most well-known application of ‘two-beam analysis’ is in the evaluation of the Burgers vectors of dislocations. A significant and well-established development in TEM was the use of multiple beams to generate phase-contrast images. This allows HRTEM lattice fringe images to be produced. Application of TEM techniques and the special adjustments that are necessary for TEM of PV materials are now described.

Conventional TEM has played an important role in the development of electronic devices, including PV heterojunctions. The method is at its most powerful when applied to a series of samples for which a growth or processing variable was adjusted. A good example is the PVD growth of CdTe/CdS⁶⁹ for which the twin density in the CdTe grains was shown to be related to the growth temperature. The twin density decreases progressively as the temperature increases through the series 425, 525 to 625°C. A second example is the evaluation of near-interface CdTe grain growth upon CdCl₂ treatment of CSS-grown CdTe/CdS/transparent conducting oxide (TCO)/glass. It is generally understood that small-grained CdTe layers undergo strain-driven grain growth upon CdCl₂ treatment, whereas large-grained material, e.g., CdTe grown at 500°C by CSS, does not.^{9–11} While the latter is true for the grains in the bulk and surface of the layer, the near-interface region shows different properties. Cousins and Durose⁶⁵ used plan-view TEM of the near-interface region of CSS-grown CdTe/CdS/TCO/glass to demonstrate that the (small) interfacial grains do undergo grain growth while the rest of the film is invariant. To do such work, plan-view TEM was essential since cross-sectional TEM would not have provided

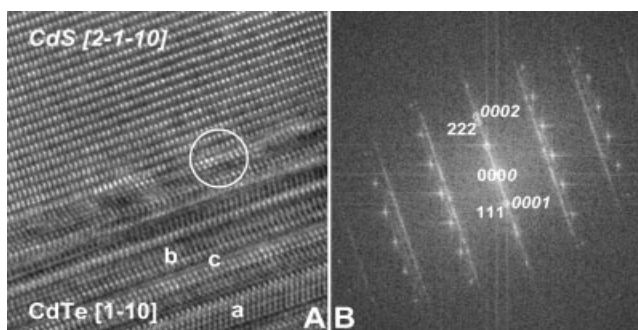


Figure 9. (A) High-resolution transmission electron micrograph of the as-deposited CdTe/CdS interface after deposition. The micrograph shows that the close-packed planes of the films are parallel with CdS [2-1-10] parallel to CdTe [1-10]. In the [1-10]-oriented CdTe layer, the two twin variants of the cubic (**a** and **b**) lattice and a localized region of hexagonal stacking (**c**) are marked. A misfit dislocation is indicated by a white circle. (B) Shows a Fourier transform of the micrograph. Diffraction spots from the CdTe and CdS layers are shown in the three- and four-digit index systems respectively, and confirm the orientational relationships. Micrograph taken from Romeo *et al.*⁷²

enough grains for a statistically valid grain-size analysis. In this particular case the sample preparation was complex and involved: (a) grinding off the glass; (b) etching off the remaining glass with HF, the TCO acting as an etch stop layer; and (c) ion beam thinning with I^+ from both sides.

HRTEM imaging and convergent electron beam diffraction of PV materials present special challenges. HRTEM and convergent electron beam diffraction require comparison of micrographs with elaborate simulations in order to be meaningful. Because of the heterogeneous nature of the materials studied, the parameters needed for simulations either cannot be obtained or are uncertain. Despite these obstacles TEM for structural investigation is called for where macroscopic measurements on thin-film solar cells require microscopic verification, e.g., copper indium gallium diselenide (CIGS)/CdS devices.⁷⁰ An example of local texture analysis by HRTEM across an as-deposited CdS/CdTe interface grown by PVD,⁷¹ is shown in Figure 9. An average [111] preferred orientation of the CdTe absorber layer was determined from XRD.⁷² With TEM, the microscopic CdTe orientation and its local dependence on the orientation of the CdS [0001] layers was studied. Where the average [111]/[0001] preferred orientation was observed locally, HRTEM imaging revealed stacking disorder, twins and dislocations within the grains (Figure 9A). By making a Fourier transform of the lattice image a local diffraction pattern for the imaged area was obtained and the lattice mismatch and the orientational relationship between CdTe and CdS were obtained.

Analytical TEM: chemical analysis

Integration of a focused-electron probe scanning attachment with TEM allows the possibility of mapping other signals from a sample and hence opens up the field of analytical TEM. Chemical information may be retrieved from the sample on account of the inelastic scattering interactions that result when electrons pass through the sample. A complete survey of the wealth of possible electron-sample interactions is available.⁶¹ EDS and EELS are probably the most popular in materials science of thin-film solar cells and often complement one another. Both rely on the energy transfer from incident electrons to core electrons of sample atoms that are thus ionized. EELS measures the number of transmitted electrons as a function of the energy loss of the incident electrons. As this energy loss depends on the shell structure of the excited atoms, it is characteristic of each chemical species. After a short dwell time, the missing electron in the core shell is replaced by an electron from a higher orbital, and the energy difference is frequently emitted as an X-ray photon. For EDS, the beam is scanned over the sample surface, and the number of photons per energy window is counted for every beam position. Thus a map of the elemental distribution across the scanned sample area is obtained. While qualitative or semi-quantitative analyses can be obtained easily, determination of absolute concentrations is difficult and requires calibration with standards of known composition. Generally, EELS has a higher spatial resolution, and can

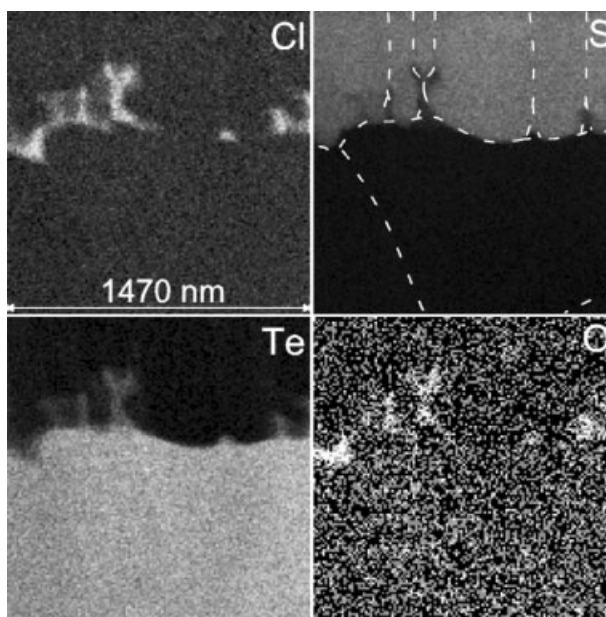


Figure 10. EDS maps of the CdTe/CdS interfacial region for a PVD-deposited CdTe/CdS/TCO/glass device after treatment with CdCl_2 . At the interface and in particular along the CdS grain boundaries the concentrations of Te, Cl and O are higher while the grain boundaries are depleted of S. In the S map, the grains are outlined along the boundaries for clarity. Maps taken from Terheggen *et al.*⁷³

reach the atomic scale, while a few nanometres are typical for EDS. In the latter case the resolution is limited by secondary-electron effects that widen the excitation volume of X-ray photons. When several elements with similar atomic numbers are present, EELS suffers from absorption-edge overlap. Signal overlap for multi-component systems is less frequent in EDS analysis. Figure 10 shows elemental maps for Cl, Te, S and O that were recorded at the interface between a CdS and CdTe layer after the sample had been annealed in a Cl atmosphere.⁷³ After the diffusion of Cl and O towards the interface, Cl segregates, owing to the low solubility in both CdTe and CdS. Considerable progress in the automatization of analytical TEM in recent years has made high-resolution analysis a standard tool in materials analysis. In combination with such new techniques as high-angular annular dark-field scanning TEM,⁷⁴ energy-filtered TEM or FIB microscopy, TEM can be expected to further and more often improve thin-film solar cell characterization.

AUGER ELECTRON SPECTROSCOPY (AES)

AES is a widely used analytical technique that provides quantitative compositional information about the surfaces of solid materials. Based on the excitation of electronic core-levels in atoms and accurate measurement of the electron energy spectrum that results from the Auger decay process, AES shares many of the attributes of a related technique, X-ray photoelectron spectroscopy (XPS). Several excellent reviews of the two experimental methods are available.^{75–80} Although the physical basis for surface sensitivity, a short (1–5 nm) electron inelastic mean free path, is the same for both methods, there are several important differences. AES typically uses electron beam excitation, and thus the study of insulators, although not impossible, is difficult.⁷⁸ While XPS is a common tool in the study of electronic structure, the convolution of several different energy levels in an Auger transition make the routine extraction of electronic information from Auger spectra impractical in most cases. In contrast to XPS, the energy resolution of AES analysers is typically not sufficient to resolve small ‘chemical shifts’ of the core levels of an element that is present in more than one chemical state.

Despite the poorer energy resolution of electron energy analysers typically used in AES relative to those used in XPS, Auger spectra, like photoelectron spectra, can be used for chemical analysis in addition to their more

common use of elemental identification. As in the case of photoelectron spectra, the core levels under scrutiny in an Auger spectrum are perturbed by their chemical environment, and can undergo chemical shifts of up to several eV. In area-averaged Auger or X-ray photoelectron spectra, resolving peaks that are closely spaced in electron kinetic energy is sometimes not possible. However, with the use of finely focused electron beams (10–15 nm) characteristic of modern AES instrumentation, the AES practitioner is frequently able to select for analysis pure phases out of a heterogeneous sample, thereby circumventing the problem of trying to energy-resolve core-level peaks that differ only as a result of chemical environments.

There are cases in which AES offers greater sensitivity to an element's chemical environment than an X-ray photoelectron spectrum. An Auger decay can involve transfer of valence electrons of a substrate to the core level of an adsorbed material, making the Auger line position of the adsorbate dependent on the adsorption site.⁷⁵ Interactions between the two core holes resulting from the Auger process ('final state' effects) can depend on an element's chemical environment, in turn making the Auger peak shape sensitive to the local chemical state. When an element's valence band is involved in an Auger transition, the energy of the transition and thus its corresponding peak position may be more sensitive to the local chemical environment than peaks resulting from photoemission.⁷⁵ A good example of this is provided by the most prominent AES and XPS lines of cadmium. The Cd 3*d* photoemission lines show only minor (~ 0.8 eV) chemical shifts in the series consisting of Cd metal, CdS and CdTe, whereas the Cd MNN Auger lines undergo substantially larger (>2 eV) chemical shifts and significant changes in line shape.^{81,82}

Several other aspects of AES are of particular concern to those working with PV materials. The high current densities ($10^4 \text{ A} \cdot \text{cm}^{-2}$) possible with field-emitter sources can cause changes in a material during analysis. Examples include the graphitization of organic substances such as those used in dye-sensitized/TiO₂ solar cells⁷⁷ and the electron-beam-induced reduction of metal oxides such as TiO₂ and ZnO.^{77,79,83} Electron-beam damage has been observed in electron-beam-induced current (EBIC) experiments on CdTe.⁸⁴ Thin stainless steel or polyimide substrates popular with PV manufacturers using 'roll-to-roll' processes can exacerbate electron-beam damage effects (A. Swartzlander, unpublished work).

The high-brightness, finely focused electron beams used in AES instruments today allow a variation on traditional AES in which two-dimensional 'maps' of Auger signals are acquired. This variant is referred to as scanning Auger microscopy (SAM). For the study of heterogeneous thin films typical of those found in PV devices, such data can be particularly useful. Figure 11, a scanning Auger micrograph of a CdTe absorber layer that had been treated with a solution of CdCl₂, is an example of how SAM can reveal information that would otherwise

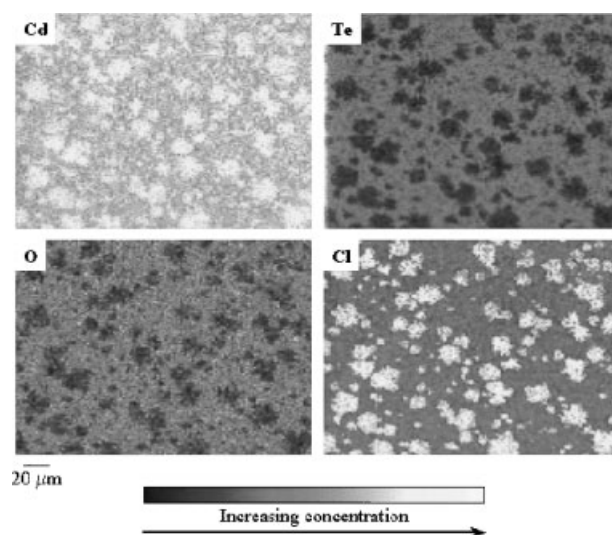


Figure 11. Scanning Auger micrograph of CdTe thin film after exposure to CdCl₂ solution and prior to thermal treatment. The CdCl₂ coverage is nonuniform and is associated with oxygen, possibly from adsorbed water or the methanol solvent. Each panel consists of a 128×128 -pixel array of elemental concentrations

be difficult to obtain. Each panel in Figure 11 consists of a 128×128 -pixel array of atomic concentrations derived from element-specific Auger transitions, with the atomic concentrations being coded in an 8-bit colour scale. The grossly nonuniform Cd and Cl coverage is too thin to be probed in plan-view by the various X-ray microanalysis techniques, and would not be directly revealed by standard XPS owing to the length scale of the Cd and Cl deposits. A labour-intensive cross-sectional TEM analysis would require many preparations to reveal the nonuniformity of the deposits, and even then they might not survive the thinning procedure.

Surface roughness common in polycrystalline absorber layers such as CdTe and Cu(In,Ga)Se₂ becomes an issue if the surface forms a buried interface for which the analyst desires AES sputter-depth-profile data. Owing to contributions from interfacial roughness, small but significant probe depths of the escaping Auger electrons, and ion-beam induced roughening and mixing, sputter-depth profiles of buried interfaces generally do not reflect the actual abruptness of the interface.^{75,85} Differences in sputter yields from element to element can distort the depth scale, usually plotted in terms of sputtering time. Methods for overcoming or minimizing these problems include the use of beams of polyatomic ions such as SF₅⁺ to minimize sputter mixing,⁸² the use of Zalar rotation to help reduce ion-beam-induced roughening⁸⁶ and cross-sectional analysis to eliminate it. Figure 12 illustrates two of these methods as used in the analysis of a CdTe-based PV device. The device structure consisted of the following: 0.14 µm metal front contact/3.0 µm CdTe/0.2 µm CdS/0.4 µm SnO₂/glass. The front contact was comprised of two metals ('metal A' and 'metal B'), arranged according to the following:

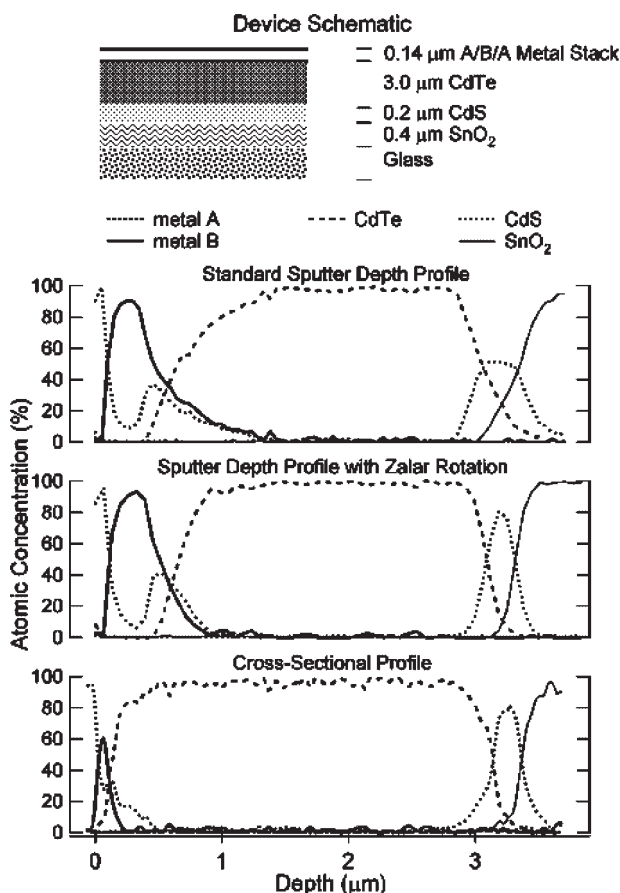


Figure 12. Comparison of AES profiling methods for a CdTe-based device. Top graph: normal sputter profile; Middle graph: sputter profile with Zalar rotation; bottom graph: cross-sectional profile. Zalar rotation gives a notable increase in the depth resolution over standard sputtering conditions. However, depth profiling has in this case apparently 'stretched' the data from the metal layers since they sputter more slowly than the underlying semiconductor. Cross-sectional profiling gives a more accurate indication of interfacial positions

0.02 μm metal A/0.1 μm metal B/0.02 μm metal A. In the upper graph of Figure 12, a standard sputter-depth profile is compared with a sputter profile with Zalar rotation (middle graph) and with a cross-sectional line profile (bottom graph). The standard sputter-depth profile greatly exaggerates the thickness of the metallization layers due to the much lower sputter rate for the metals than for CdTe and CdS. In addition, a combination of intrinsic sample roughness, sputter mixing and sputter-induced roughening leads to an apparent broadening of the interfaces. Continuous rotation of the sample during analysis (known as Zalar rotation when the sample must be continually displaced in the x - y plane to keep the sputter crater coincident with the analysis point) improves the depth resolution of the profile by minimizing artifacts caused by sample roughness and sputter-induced roughening. As can be seen in the middle graph of Figure 12, the interfaces appear somewhat sharper, and individual layers are better resolved. Nevertheless, the overall distortion of the depth profile due to the comparatively low sputter rate of the metal layers is still evident.

Because a cross-sectional line profile does not rely on sputtering to access the interior regions of a sample, it is not subject to artifacts that are encountered with sputter-depth profiling. This is demonstrated in the lower plot of Figure 12. In this case, the width of the metallization layer is undistorted, and the spatial resolution of a cross-sectional line profile is limited only by the spatial resolution of the electron gun used as the excitation source and by mechanical vibrations of the instrument.

AES is a technique characterized by a unique combination of high spatial resolution and high sensitivity to surface composition and will continue to play a large role in the characterization and understanding of PV materials. There are several variations on the technique that have not been exploited by the PV community, but perhaps will become important in the future, including: (1) using a 'core hole clock', ultra-fast charge-transfer dynamics may be studied on the sub-femtosecond timescale using AES in conjunction with other core-level spectroscopies;⁸⁷ (2) the use of high-resolution AES measurements to extract information on semiconductor electronic structure, including electron correlation effects and screening density of states;⁸⁸ (3) *in situ* compositional analysis of growing films by using the electron beam from a reflection high-energy electron diffraction (RHEED) setup⁸⁹ as an Auger excitation source; and (4) the determination of surface structure via Auger electron diffraction (AED), a technique involving the analysis of diffraction patterns formed by outgoing Auger electrons.^{90,91}

SECONDARY-ION MASS SPECTROMETRY (SIMS)

SIMS is an extremely sensitive technique for analysing surface and near-surface regions of solid materials. It is an established method within the semiconductor industry for studying the distribution of dopants and contaminants in microelectronic materials and devices. The basic principle is that multi-layer structures are analysed by eroding (sputtering) them using a focused ion (primary) beam. Ions ejected by this process (the secondary ions) are then analysed for mass/charge ratio using a mass spectrometer. In contrast to the mass spectroscopy methods used for bulk analysis, which require dissolution of the sample, SIMS allows for depth-resolved information to be obtained from layered structures, including electronic devices. Several excellent books cover the technique.⁹²⁻⁹⁶ The features that make SIMS attractive as an analytical tool (sensitivity, depth resolution and elemental specificity) may also lead to artifacts that make it difficult to interpret the data (lateral inhomogeneities, surface topography and variations in ion yield). In spite of these difficulties, SIMS is often the only analytical tool able to probe low elemental concentrations within the layers of thin-film materials and devices. The following section gives a brief overview of the SIMS technique, followed by discussion of several examples illustrating the utility of SIMS for thin-film PV analysis.

The SIMS experiment can be performed in the dynamic or static mode. In both cases, the sample surface is bombarded with a focused beam of primary ions, generally oxygen, caesium, gallium or argon, at energies ranging from approximately 500 eV to 15 keV. The difference between a dynamic or static SIMS measurement is the total dose of primary ions impinging on the sample surface. The static limit is defined by the total primary ion dose, which must remain below 10^{13} primary ions/cm². The primary ion beam must remove and subsequently ionize the sputtered material, a highly inefficient process with ion yields varying by orders of magnitude. The ionization process is intimately linked to the chemistry of the host matrix and the chemistry of the

element of interest in this matrix. However, the energetic process used to produce the secondary ions destroys the surface order, and thus for dynamic SIMS measurements the cluster ions observed among the ejected particles do not necessarily represent the original chemistry of the surface. This means that the dynamic SIMS process, although being highly sensitive to materials chemistry, does not provide a direct probe of that chemistry. SIMS differs from other surface-analysis techniques in that it is a mass-spectrometry-based technique, which allows for the study of all elements in the periodic table, including H and D (^2H), as well as the isotopes. It is sensitive over an extraordinary range of concentrations—more than eight orders of magnitude. If quantitative results are desired, the variability of the secondary ion yield dictates that closely matched standards be used for each element/matrix combination studied. For elemental concentrations below ~ 1 at. % in a given matrix, the change of signal level for a given element is linear with the change in concentration; thus, even though standards are necessary, only one standard is needed for concentrations ranging over more than six orders of magnitude. Owing to the high dynamic range SIMS data is generally displayed on a logarithmic axis. Data are collected in one of three modes, as mass spectra, as depth profiles or as a function of position in the form of an elemental ion image. By far the most common method of data acquisition for thin-film analysis is the dynamic SIMS depth profile, in which specific masses are studied as a function of sputter time. By measuring the depth of the ion-beam-milled crater with a profilometer, it is possible to convert sputter time to depth. The following examples are all based on dynamic SIMS experiments.

One capability of SIMS that is unique among the standard depth-profiling tools is the ability to perform direct measurements of H distributions in materials. In addition, because SIMS has the ability to study isotopes, it is also possible to perform studies with deuterium. The following example is taken from research in the amorphous-Si area. The study of H diffusion in the a-Si:H lattice is important for understanding and controlling the stability of these materials. In this example, a special test structure was grown on a c-Si substrate with a layer of deuterated a-Si:H sandwiched between two standard hydrogenated layers. The test structure was used to study the effect of various conditions of temperature and illumination on the diffusion of D (and by analogy H). Figure 13 shows several D depth profiles taken from different pieces of the structure after they were subjected to 240°C in the dark for times ranging from 1 h to 16 days. It is immediately evident from the profiles that D diffuses away from the internal layer as a function of time. This approach has been used successfully to derive diffusion constants for D and H in a-Si:H.^{97,98}

There are several other points that are worth noting in Figure 13. First, the SIMS technique is extremely reproducible when conditions are properly controlled. The data for this figure were taken from four different samples, yet the precision is so high that the small amount of diffusion between the 1- and 3-h sample may be discerned at the leading (left-hand) edge of the test structure. Second, in this example, the surface roughness of the sample was not the limiting factor for the depth resolution; thus, it is also possible to make observations about diffusion that occurred during growth of the sample, shown by the left-hand interface of the test structure being sharper than the right-hand one. Finally, there is information about the depth resolution of the SIMS

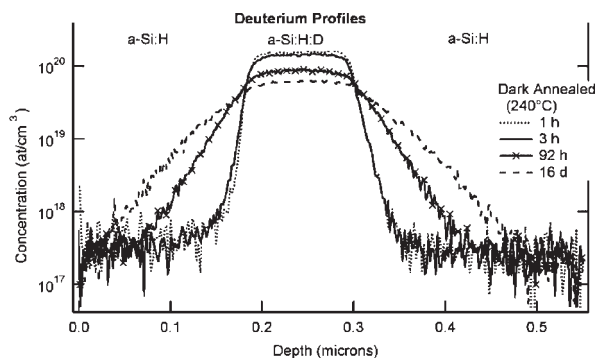


Figure 13. SIMS deuterium depth profiles obtained from different pieces of a sandwich amorphous silicon test structure (a-Si:H/a-Si:H:D/a-Si:H/c-Si) subjected to dark annealing at 240°C for 1 h, 3 h, 92 h and 16 days. Use of the deuterium has allowed diffusion to be monitored to a high degree of accuracy and reliability

measurement itself. No difference in diffusion is observed between the 1- and 3-h samples at the trailing (right-hand) edge of the test structure. This is because small amounts of diffusion are obscured by sputter-induced mixing resulting from the impact of the primary ions. Analysis of the same samples at lower primary energy showed definite improvement in the sharpness of the trailing edge.

Studying the depth and lateral distributions of trace elements (i.e. <1 at. %) in thin films is necessary for understanding the physical and electrical properties of these materials. It is commonly accepted that the incorporation of some amount of Cu into CdTe/CdS through the back contact improves the performance of the device. However, Cu is also linked to potential instabilities in the device. The power of SIMS to study the distribution of Cu has been recognized by several groups.^{99,103} In this example, SIMS was used to measure the effect of various processing steps on the amount of Cu in the CdTe/CdS device. The samples came from vapour transport deposited CdTe/CdS on commercial SnO₂-coated soda-lime glass. Pieces for analysis were gathered after various processing steps and included as grown, after wet CdCl₂ treatment, and after contacting with the standard process used at the National Renewable Energy Laboratory (NREL; Golden, CO, USA).¹⁰⁴ The SIMS profiles were performed under high mass resolution to separate the Cu signal from the Te²⁺ that appears at the same nominal mass.¹⁰⁵ This also removed the interference of O₂⁺ from the ³²S signal and the ³⁴SH signal from the ³⁵Cl signal. Figure 14 shows the raw depth-profile data for Cd and Cu (Figure 14a) and the quantified data for Cu (Figure 14b). The steps to arrive at Figure 14(b) from Figure 14(a) are illustrative of several important points for the SIMS analysis of these materials.

The first point to note in the profiles shown in Figure 14(a) is that the surface roughness and sputter-induced topography causes the CdS layer to appear significantly thicker than the targeted thickness of ~0.3 µm. Sputter-induced roughening is reduced in this work by analysing with an oxygen primary beam instead of Cs. Despite the relatively poor depth resolution, it is still possible to determine the location of the CdS layer and to observe the interfaces between layers. The 'raw' data, however, are still not quite raw; rather they have been normalized to the ¹¹¹Cd signal to remove variations in the secondary ion signal that might result from any changes in the primary ion current between analyses. This process is performed on almost all SIMS data that

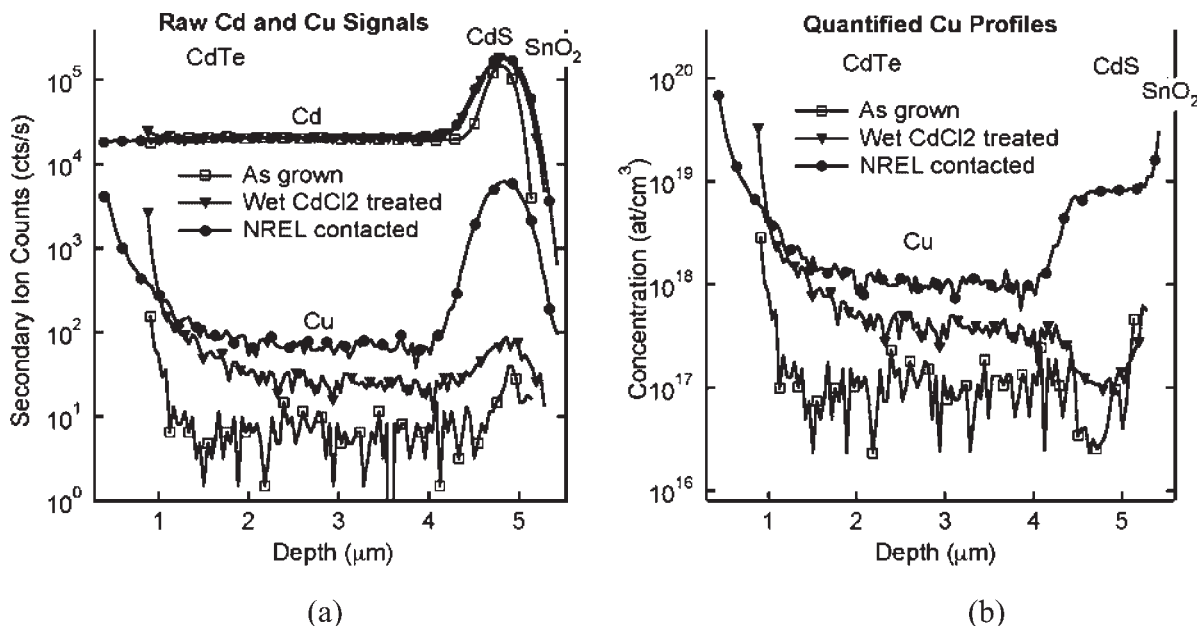


Figure 14. Comparison of the raw and corrected Cu depth profiles from three CdTe/CdS thin-film device materials, as grown, after wet CdCl₂ processing, and after application of a back contact. The comparison highlights the need to make proper quantified measurements. The data in (a) are raw, normalized to the Cd signal in the CdTe only. The data in (b) have been corrected by using ion-implanted standards of both CdTe and CdS to yield Cu concentrations in at./cm³. Significantly, the concentration of Cu is only greater in the CdS for the sample contacted with a Cu process

are not quantified with external standards. Normalization to an internal reference signal facilitates the direct comparison of different profiles within the same material, and allows for a relative determination of the differences between samples. In this case, the normalized data show a steady increase in the level of Cu in the CdTe and CdS as additional processing steps are applied, indicating that measurable Cu is added not only during the contacting step but also during the CdCl₂ step.

From the raw data in Figure 14(a), there also appears to be a significant amount of Cu being added to the CdS at each step. This increase is also noted in signals from other elements such as Cl (not shown here). However, a comparable increase in the Cd signal is also apparent as the profile reaches the CdS, indicating a change in some physical parameter as a result of the different matrix. Careful measurements of the sputter rate indicate a slight increase in the rate in the CdS relative to the CdTe. Increasing the sputter rate will increase the overall number of secondary ions, resulting in higher signal levels for all elements. A truer picture of the change in signals between the CdTe and CdS can be obtained by normalizing the Cu point by point to the Cd signal. This is also done during the conversion of the ion signals in Figure 14(a) to the concentrations in Figure 14(b) through the use of relative sensitivity factors for Cu in CdTe and Cu in CdS. A separate relative sensitivity factor must be determined for each matrix. Relative sensitivity factors s are determined from suitable ion-implant reference materials, which in this case is ⁶³Cu implanted into single-crystal CdS and single-crystal and polycrystalline CdTe. The quantified data in Figure 14(b) show that when the correction for sputter rate and differences in ion yield are removed, the Cu level in the CdS is actually lower than that of the CdTe for all but the contacted sample. The increase in the quantified Cu levels at the CdS/SnO₂ interface are the result of using the Cd signal for reference. As with many experiments, the data do not tell the entire story. The SIMS measurement provides the total amount of Cu in the films, but still needs information about the carrier concentration to determine the electrically active fraction. The carrier concentration must be gleaned from a different technique. SIMS does supply proof that Cu is actually present in the device and at what overall level.

Although SIMS is best suited for analysis of trace quantities in materials, its ability to measure the properties of the bulk matrix simultaneously with the trace impurities is appealing. The SIMS measurement does measure signals from the matrix. Indeed, as discussed above, matrix signals are used as internal references for most quantitative work. What is difficult with SIMS is to relate the change in ion signal to changes in concentration for elements that are present at levels over the dilute limit of ~ 1 at.%. One method that has been used successfully in the analysis of other semiconductor materials (e.g., SiGe, and AlGaAs alloys) is the analysis of molecular ions comprising the element of interest (M) and Cs, the $(M + Cs)^+$ cluster ions. This method, which uses Cs as the primary ion species, has been shown to reduce or eliminate the change in secondary ion yield in going from one matrix to another. The theory is that sputtering and ionization are decoupled, leading to a lesser effect of the sample chemistry on secondary ion yields.¹⁰⁶ In this example, the $M + Cs$ technique is compared with the results from an AES profile.

The data in Figure 15 were obtained from CIGS grown by a three-stage process on Mo-coated soda lime glass.¹⁰⁷ The molecular ion data in Figure 15(a) are typical for this type of analysis. The grading in Ga is clearly visible, whereas the other signals are essentially flat on a logarithmic scale. In contrast, the AES profile is displayed from 0 to 100 at.% and appears to show significantly more grading (Figure 15b). Figure 15(b) also shows the superposition on the AES data and the SIMS data. In this figure, the only change to the SIMS signals is to apply a linear correction factor. The correspondence between the SIMS and AES data is striking. Similar results are obtained for materials containing S in addition to Se. Appropriately scaled molecular ion data can be used to generate bandgap-grading profiles for numerical modelling (A. Rockett, personal communication at NCPV National Thin Film Team Meeting, 2001).

In this brief discussion it has not been possible to address the many uses of SIMS for the study of thin-film materials and devices, and there are many omissions. Neither has there been space to address several important areas of SIMS research, including static SIMS for the study of organic molecular species on surfaces, and the exciting upcoming high-lateral-resolution instruments that may be able to answer questions about impurities in grains versus grain boundaries. Static SIMS has seen broad application to the areas of polymers and adhesion science; however, limited effort has gone into studying inorganic species emitted from surfaces. This area will probably expand in the future. Likewise, another area that will be a force for thin films is the advent of high-brightness, small-spot ion sources. Currently, there is at least one instrument that has lateral resolutions in the

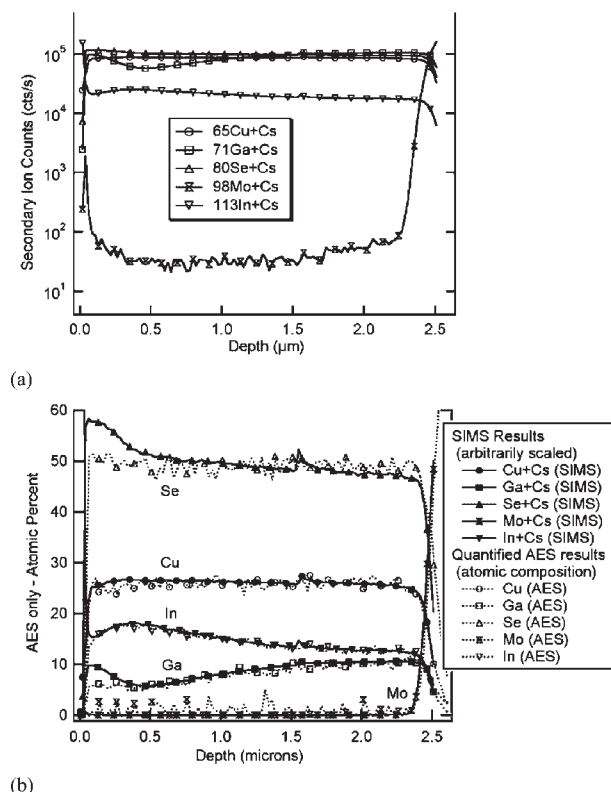


Figure 15. Comparison between a SIMS depth profile acquired with molecular ions $(\text{M} + \text{Cs})^+$ with an AES depth profile, both taken from a CIGS film grown on Mo/SLG. (a) The raw SIMS profile data are plotted as a function of depth; (b) the SIMS data rescaled and displayed against an AES depth profile from the same sample. The vertical axis is applicable to the AES data only. The correlation between the molecular ion cluster SIMS and the AES is very close. Both reveal Ga grading that is significant to tuning the performance of the PV devices

sub-100 nm range with sensitivities of parts per million. It is not difficult to imagine what could be done with this combination.

In conclusion, SIMS is a versatile tool for the study of trace elements and contaminants in thin-film materials. It is routinely used to study trace quantities in thin-film materials, in both a qualitative and quantitative manner. It provides direct insight into elemental constituents that affect the performance of thin films. One of the problems for SIMS analysis of thin-film materials is that, even when it is possible to measure a given quantity, it is sometimes not possible to determine what the result really means. It is likely that additional research will result in better understanding of the factors that affect the measurement, leading to improved consistency of results.

PHOTOELECTRON SPECTROSCOPY AND RELATED TECHNIQUES

The performance of thin-film solar cells is strongly determined by the electronic properties of the heterointerfaces involved. The important quantities are the energetic and spatial distributions of the density of interfaces states and defects as well as the alignment of energy bands and the contact potential distribution.^{108,109} The electric response of the device can be easily deduced from standard electric and optoelectronic measurement techniques, but it is very hard to identify the origin of a given response to changes in the structure and composition of the interface on an atomistic level, which are dependent on given preparation and processing conditions. Usually the interface in most optimized thin-film solar cells turns out to be much more complex, as found for idealized physical models, and therefore no predictions can be easily drawn from the given and accepted

theories of heterojunction formation. Book reviews are available for the electron spectroscopies, such as photoelectron spectroscopy, using different excitation sources (XPS, ultraviolet photoelectron spectroscopy, UPS and soft X-ray photoelectron spectroscopy, SXPS),^{75,110,111} X-ray-absorption spectroscopy (XAS) and X-ray emission spectroscopy (XES; near-edge X-ray absorption fine structure, NEXAFS and extended X-ray absorption fine structure, EXAFS),^{112,113} as well as Auger spectroscopy.⁷⁵ Collectively these techniques provide versatile tools for surface-sensitive experiments which may also provide information on lateral inhomogeneities using, for example, photoelectron emission microscopy (PEEM), microelectron spectroscopy for chemical analysis (μ -ESCA) or μ -NEXAFS.^{106,114} The high surface sensitivity allows us to obtain detailed spectroscopic information on a sub-monolayer level, but also leads to experimental problems as buried interfaces cannot be studied readily. Therefore sophisticated experimental set-ups and procedures must be developed to approach the surface and interface properties of semiconductors.

For this purpose we have built up integrated ultra-high vacuum preparation and analysis systems, as shown in Figure 16. The systems allow the analysis of semiconductor and device surfaces in their supplied state (i.e., after *ex situ* preparation), but these surfaces may deteriorate, and their properties modified under ambient conditions. It is also possible to perform back-engineering of completely processed solar cells for example by etching and sputtering to uncover the interfaces of interest. In this case the applied recipes must always be checked very carefully to ascertain how far they will disturb the interface and materials properties given originally. In the most promising approach the films and interfaces are prepared *in situ* following the given solar cell technology and their properties analysed after every step. However, this approach is very time consuming and expensive and the equivalency of the preparation and processing sequences to the cell technology should be checked by simultaneously performed electric and optical measurements.

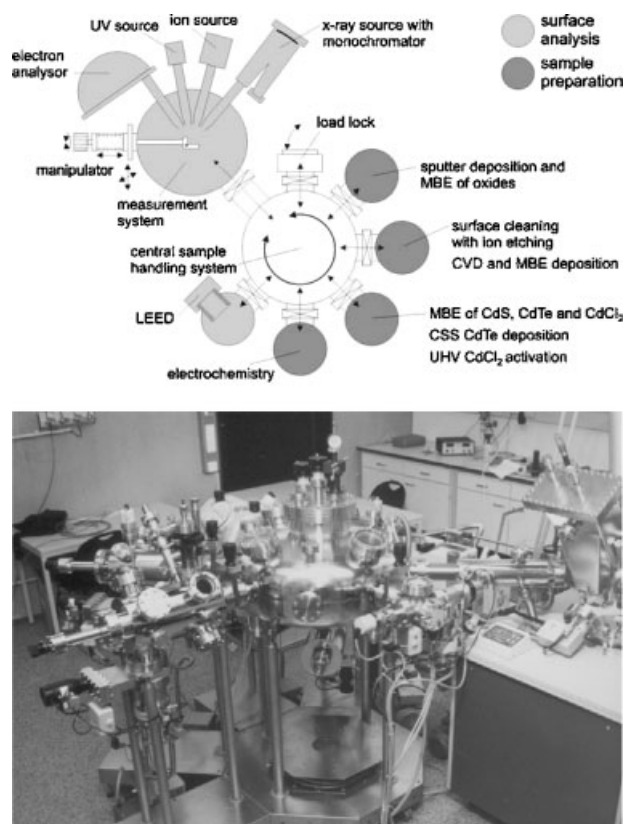


Figure 16. Layout (upper panel) and realization (lower panel) of the integrated surface analysis and preparation system DAISY-MAT in Darmstadt, Germany. CVD, chemical vapour deposition; LEED, low-energy electron diffraction; UPS, ultraviolet photoelectron spectroscopy; MBE, molecular beam epitaxy

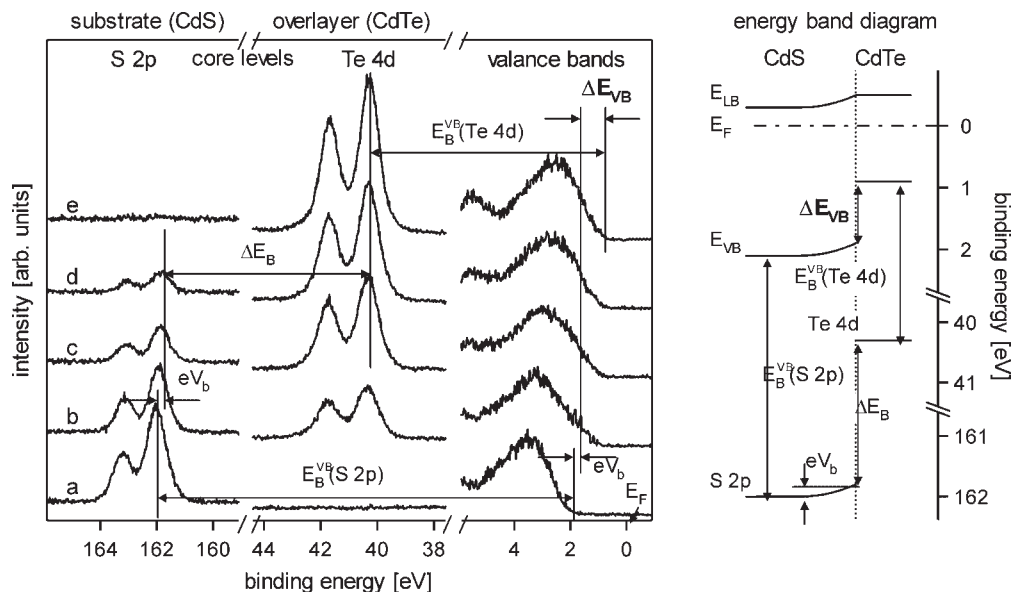


Figure 17. Photoelectron spectra of step-by-step CdTe/CdS interface formation and deduced energy band diagram. See text for an explanation of the sequential deposition steps represented by spectra a–e

The type of information which can be obtained will be presented by a typical experiment, as has been performed to investigate the CdS/CdTe heterointerface (Figure 17). The starting point is a CdS thin film that has been deposited by PVD on to a TCO substrate (Figure 17, spectrum a). The composition of the CdS film can be checked by XPS and may be compared with samples prepared outside the ultra-high vacuum system showing contaminations or with samples treated in a different way using annealing steps; CdCl₂ activation steps, electrodeposition, etc. The electronic properties can be deduced from the position of the valence band edge in the valence band spectra giving the surface position of the Fermi level ($E_F - E_{VB}$) and the secondary electron onset giving the work function ϕ . These quantities can also be deduced from the binding energies of the core lines when the energy difference $E_{VB} - E_{core}$ (E_B^{VB}) is known from reference measurements. In this case the CdS is *n*-doped with E_F 0.4 eV below the conduction band. *A priori* it is not known if flat band conditions are given as assumed for this case or if the surface Fermi level position deviates from the bulk position due to surface-band bending induced by intrinsic or extrinsic surface states. In such cases independent experiments on semiconductor bulk doping are needed or surface photovoltage experiments looking for bias light-induced shifts of photoemission spectra may be performed.^{115,116} Spectra (b–e) in Figure 17 show the changes in the spectra induced by a PVD step-by-step deposition of a CdTe over-layer at room temperature. In this case no interface reaction occurs, therefore the core level lines and valence band features are superpositions of the CdS and CdTe emission features. Interface reactions and interdiffusions, which also may be induced at the CdS/CdTe interface by CdCl₂ activation, will lead to chemical shifts of the core lines as well as to changes in the relative intensity of the composite lines. Owing to CdTe deposition the CdS substrate lines move due to CdTe-induced band bending (eV_b) and the overall shift amounts to 0.3 eV. With the known value for band bending, the known values of E_B^{VB} (the value for the CdTe can be deduced from the thick CdTe layer; Figure 17, spectrum e), the band alignment can be calculated as also shown in Figure 17. With the known values of the Fermi level position, the measurements of the work function and literature value of bandgaps, the band energy diagram of the device is given. Deviations in band alignment from the electron affinity rule¹¹⁷ due to the given interface structure will lead to changes in the distribution of charges (electronic or ionic) across the phase boundary, which are evident from the related electric potential steps δ in the alignment of the vacuum levels. In practice the interface may be much more complex than shown in this rather simple example and the spectral information must be very carefully interpreted to obtain reasonable conclusions.

High-quality spectral data are a precondition for reliable results; usually all available emission lines should be measured with high precision and should be interpreted in a consistent way (sometimes the Auger lines provide better information on chemical shifts). For the CdTe solar cells, interdiffusion at the SnO₂/CdS and CdS/CdTe interface has been observed.^{118,119} Also the electronic properties of ultrathin films of II–VI semiconductors have been shown to be modified, probably owing to strained growth.^{120,121} At CIGS/CdS interfaces modified interface properties have also been deduced from interdiffusion and/or the formation of a Cu-deficient chalcopyrite substrate (ordered defect or ordered vacancy compound interface).^{121–125} In this case it is very helpful also to use other techniques such as XES,^{126,127} which can also be used for the investigation of buried interfaces, and inverse photoemission,¹²⁸ which gives direct experimental information on the position of the conduction band edge. A number of investigations have recently been performed to investigate the effects of wet chemical processing steps which so far are of crucial importance for the CIGS front-contact formation (CdS CBD)^{127,129} as well as for the CdTe back-contact formation (wet chemical etching).¹³⁰ In addition, studies on the interface properties of injection solar cells with TiO₂ as the semiconductor substrate have been performed.^{131,132}

In summary, the application of surface-sensitive techniques such as photoelectron spectroscopy may provide very detailed information on the interface properties of thin-film solar cells. A clear correlation of chemical and structural effects and their electronic consequences may be deduced at the atomistic level. However, care must be taken to obtain reliable results, which may be achieved by comparing samples prepared in a different way and by combining the surface-sensitive experiments with electrical and optical measurements.

PHOTOLUMINESCENCE (PL)

PL spectroscopy provides a rapid, non-destructive method to characterize the electronic properties of the polycrystalline semiconductors used in thin-film PVs.¹³³ Ease of measurement makes PL a good choice for quick evaluation of relative material quality, including carrier lifetime, purity and degree of crystallinity, through evaluation of PL intensity, peak energy and linewidth, respectively.¹³⁴ PL spectroscopy is well suited for identifying shallow impurities and defects through the energy, injection density and temperature dependence of the PL spectrum.^{135,136} Photoluminescence excitation spectroscopy (PLE) provides information on the absorption spectrum in samples where transmission measurements are not possible.¹³⁷ Excellent discussions on the mechanisms of PL in semiconductors are provided by Pankove,¹³⁸ and by Yu and Cardona.¹³⁹ Gilliland has written an extraordinarily comprehensive review of PL in crystalline semiconductors with an emphasis on the experimental aspects.¹⁴⁰

Instrumentation is generally assembled as a custom system from commercially available components, as there are few complete commercial systems available. There are four basic components that make up a PL measurement system. First is a source of optical excitation, generally a high-brightness monochromatic source such as a laser. Next is a sample holder and optics that provide for focusing the laser on to the sample surface, and optics to collect and image the PL into a spectrometer. The spectrometer or monochromator comprises the third basic component, and can be as simple as a system of filters or a prism, but is generally either a scanning or fixed-grating monochromator, depending on the fourth element, the optical detector. PMTs provide extremely high sensitivity, capable of single-photon detection, and require a scanning monochromator to sequentially step through the spectral range of interest. Diode arrays or CCDs now rival PMTs in quantum efficiency, and achieve parallel detection of the entire spectrum at once, permitting long integration times to achieve high signal-to-noise ratios, or very fast data acquisition for samples with adequate PL intensity. The system is completed with the addition of a desktop computer for instrument control and data acquisition and analysis.

Polycrystalline thin films of CdTe and CIGS present unique challenges for PL characterization. The high concentration of grain boundaries, defects and impurities typical of thin-film PVs produce broad linewidths, and the spectra are frequently dominated by sub-bandgap recombination through defects and impurities. High non-radiative recombination rates often require that measurements be performed at cryogenic temperatures. Figure 18 shows low-temperature PL spectra for (Figure 18a) a CdTe solar cell and (Figure 18b) a CIGS absorber layer. The CdTe spectrum can be divided into three regions: (a) bound-exciton transitions from

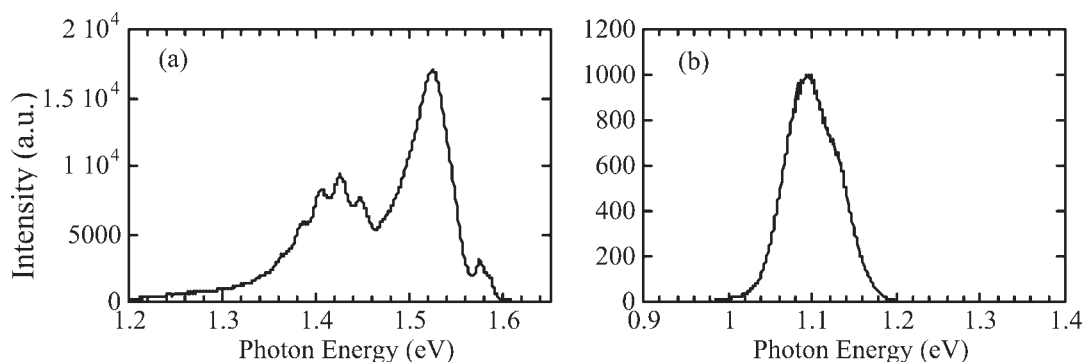


Figure 18. (a) 10 K PL spectrum for a polycrystalline CdTe/CdS solar cell excited by an HeNe laser on the back surface of the absorber; (b) 4.2 K PL spectrum for a CIGS absorber layer prior to CdS deposition¹⁴¹

1.58 to 1.60 eV, (b) a broad donor–acceptor pair transition at 1.53 eV and (c) a broad defect band with multiple phonon replicas ranging from 1.34 to 1.46 eV.¹⁴² Defects in CIGS tend to form energy bands, as evidenced by the lack of structure in the PL spectrum for a 0.26 at.% Ga CIGS film in Figure 1(b). The broad peak at 1.1 eV is identified as a bound-exciton transition. PL spectra for CIGS films depend strongly on composition and film processing.¹⁴³

PL is also quite useful in characterizing the electronic states of hydrogenated amorphous silicon (a-Si:H).¹⁴⁴ PL emission is dominated by band-to-band recombination, with a broad peak in the 1.2–1.4 eV energy range. The energy of the peak in the PL spectrum is affected by hydrogen content and degree of crystallinity. Yue and co-workers have demonstrated the usefulness of PL spectroscopy in studying the amorphous-to-microcrystalline transition in Si:H.¹⁴⁵

Time-resolved photoluminescence (TRPL)

TRPL measures PL intensity as a function of time. This popular measurement is used in numerous disciplines and takes many experimental forms. For thin-film PV characterization, most measurements use a fast laser pulse to excite electrons in the semiconductor. A portion of the emitted PL is collected optically and directed to a fast detector, generally through optical filters and monochromators that limit the amount of laser light and extraneous light that reaches the detector. The PL intensity can be measured directly as a function of time by a photodiode or a streak camera; however, to attain a higher signal-to-noise ratio and faster time resolution, clever techniques, such as single-photon counting and pump and probe, are commonly used. In single-photon counting, the time it takes for a PL photon to reach the PMT after an excitation laser pulse is measured with a time-to-amplitude converter and stored in a multichannel analyser. The experiment is repeated many times with a high-repetition-rate laser, and a histogram is built indicating when the first photon arrived for many (often more than a million) excitation pulses. Provided that the experiment is done under certain statistical conditions, this histogram will represent the PL intensity as a function of time. In the up-conversion technique, a beam of laser pulses is split into a pump pulse and an up-convert pulse. Semiconductor PL excited by the pump pulse is collected, collimated and focused on to a nonlinear crystal such as β -barium borate or lithium iodate. The up-converted laser pulse is also focused on to the nonlinear crystal in a noncolinear alignment to generate the sum-frequency mixing of the up-convert beam with the PL. A PMT and monochromator are configured to detect photons at the sum frequency ($\nu_{\text{laser}} + \nu_{\text{PL}}$) of the up-convert pulse and the PL, resulting in a measure of the PL intensity with a time resolution on the order of the laser pulsewidth. Varying the relative delay between the pump and up-convert pulses by using an optical delay stage allows measurement of the time dependence of the PL. More detailed descriptions of these and other TRPL techniques can be found in the classic text by O'Connor and Phillips.¹⁴⁶ The PL decay rate depends primarily on the rates of Shockley–Read–Hall, radiative and Auger recombination in the bulk, and recombination at the grain boundaries, interfaces and surfaces of the

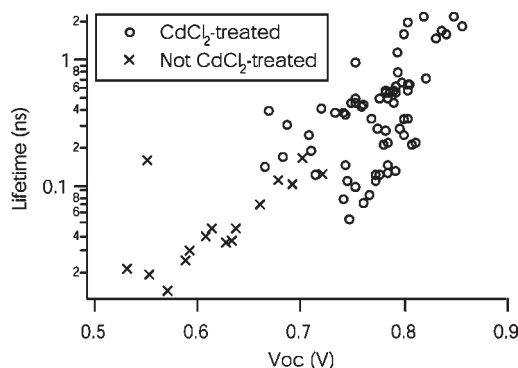


Figure 19. TRPL lifetime versus open-circuit voltage V_{oc} for CdTe cells with closed-space sublimation deposition and various post-growth processing conditions. Data include values from several studies in the literature¹⁴⁸

sample.¹⁴⁷ By understanding and measuring recombination as a function of temperature, free-carrier concentration, injection level, sample dimensions and sample properties, it is possible to assess material quality and the roles of the different recombination mechanisms on solar cell performance.¹⁴⁸

Nearly all direct lifetime measurements on polycrystalline CdTe have been done with TRPL. Most measurements have been made on completed CdS/CdTe junctions, with the excitation light incident on either the glass or the bare CdTe surface. The excitation light typically has an absorption length of several hundred nanometres; hence, measurements through the glass are affected by junction effects and interface quality, and measurements on the CdTe surface may be affected by free-surface recombination. Room-temperature lifetimes on the back surface typically range from 200 to 500 ps for CdCl₂-treated samples, and from 10 to 200 ps for untreated samples.^{149,150} Lifetimes measured at the CdS/CdTe interface are illustrated in Figure 19, which indicates a strong correlation of PL lifetime with open-circuit voltage.¹⁴⁸

Among the handful of lifetime experiments performed on CIGS, most experiments used TRPL, and all used excitation light with a short penetration depth. Two research groups, one using TRPL and the other dual-beam optical modulation, report room-temperature lifetimes as high as a few nanoseconds on bare untreated absorber films, and a large increase in the lifetime measured on corresponding CIGS/CdS junctions.^{140,151,152} Another group, under very high injection conditions, report room-temperature TRPL lifetimes on bare absorber layers ranging from 5 to 55 ns.^{153,154} Three articles show a correlation between CIGS lifetime values and open-circuit voltage.^{140,152,153}

For both CdTe and CIGS, it is generally believed that Shockley–Read–Hall-type recombination is dominant; but extensive work remains to separate and characterize the roles of grain-boundary, free-surface, interface and intragrain recombination.

PL decay curves from amorphous Si are highly non-exponential and temperature-dependent. Single-exponential fits on different sections of one decay curve often produce lifetime values that start at a few nanoseconds and increase many orders of magnitude. This behaviour is attributed to trapping in localized states and recombination by radiative tunnelling.¹⁴³

ELECTRON-BEAM-INDUCED CURRENT (EBIC)

Connection of electronic devices to an amplifier while under the interrogation of the electron beam of an SEM permits charge-collection microscopy, also known as the EBIC technique. The term EBIC is used generally to represent a collection of techniques based on measurement of: (a) minority, i.e., ‘injected’ carriers generated by energy deposition by a primary beam; and/or (b) the flow of the primary beam current itself, the latter being less common. Since electron beams may be focused and EBIC utilizes minority carriers, the potential of the technique for studying thin-film solar cells with sub-grain scale resolution was recognized early on. Interpretation of all EBIC techniques demands an appreciation of the generation of charge carriers by an electron beam and their

collection—or else loss—in a device. While much can be gained from qualitative interpretation, this is often underpinned by modelling, not least of the electron–hole pair generation function in a multiplayer structure. This can be achieved on a desktop computer with little computational effort.¹⁵⁵ For reviews of the EBIC technique in general the reader is referred to reviews and books.^{156–158} Grain-boundary EBIC (‘remote’ EBIC) is described in an early paper by Russell *et al.*,¹⁵⁹ later in more detail,^{160,161} and with application to solar cell materials.¹⁶²

Best known among the EBIC techniques is the cross-section or lifetime curve method; the device is cleaved and the beam scanned perpendicular to the layer stack. The induced current response is measured as the beam traverses the depletion region. Ideally this takes the form:

$$I_{\text{EBIC}} = I_0 \exp(-|x|/L)$$

where x is the distance from the junction, I_0 a constant and L the minority-carrier diffusion length for electrons or holes. Cross-section EBIC therefore allows the junction position and homogeneity to be seen and the minority-carrier diffusion length to be measured. However, there are some confounding factors for interpretation in the case of thin-film solar cells and some of these are now listed. For CdTe/CdS Kenny and McClure¹⁶³ found non-ideal line shapes that could not be modelled by including surface recombination or high injection; Poor cleaving technique is thought to give spurious results—this can be overcome by clipping samples with electrical pliers rather than by breaking scribed glass. Grain boundaries make the profiles complex. The injection bulb has a finite size that may be comparable with the minority-carrier diffusion length. Rechid *et al.*¹⁶⁴ show how the collection function may be deconvoluted from the EBIC signal. The same authors highlight another systematic effect; the line shape can be altered by the generation of charge in the depletion region by X-rays (and cathodoluminescence) that are themselves generated when the electron beam impacts on *other* parts of the cell, e.g. the glass substrate. An example from the CdTe/CdS materials system is shown in Figure 20. The principal peak is due to junction EBIC response while the peak on the left apparently originates from the (non-active!) glass substrate. Rechid *et al.*¹⁶⁴ explain how the true junction response may be deconvoluted from the total envelope.

Control of the accelerating voltage in an SEM allows depth-dependent information to be obtained from a sample. For the case of thin-film solar cells the quantity of interest is the collection function $F(z)$. The (voltage-dependent) EBIC signal is:

$$I_{\text{EBIC}} = \int_0^{\infty} g(z)F(z)dz$$

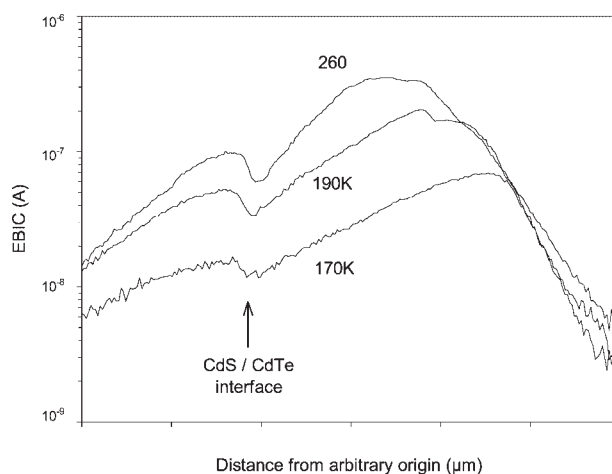


Figure 20. Cross-section EBIC response curves for a CdTe/CdS/TCO/glass cell as a function of temperature¹⁶⁵. The main peak is from the junction, the left-hand peak arises from radiation by the glass substrate that itself generates carriers at the collecting junction¹⁶⁴

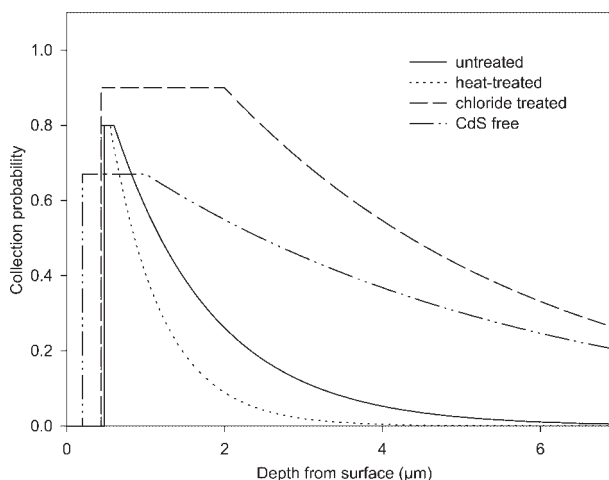


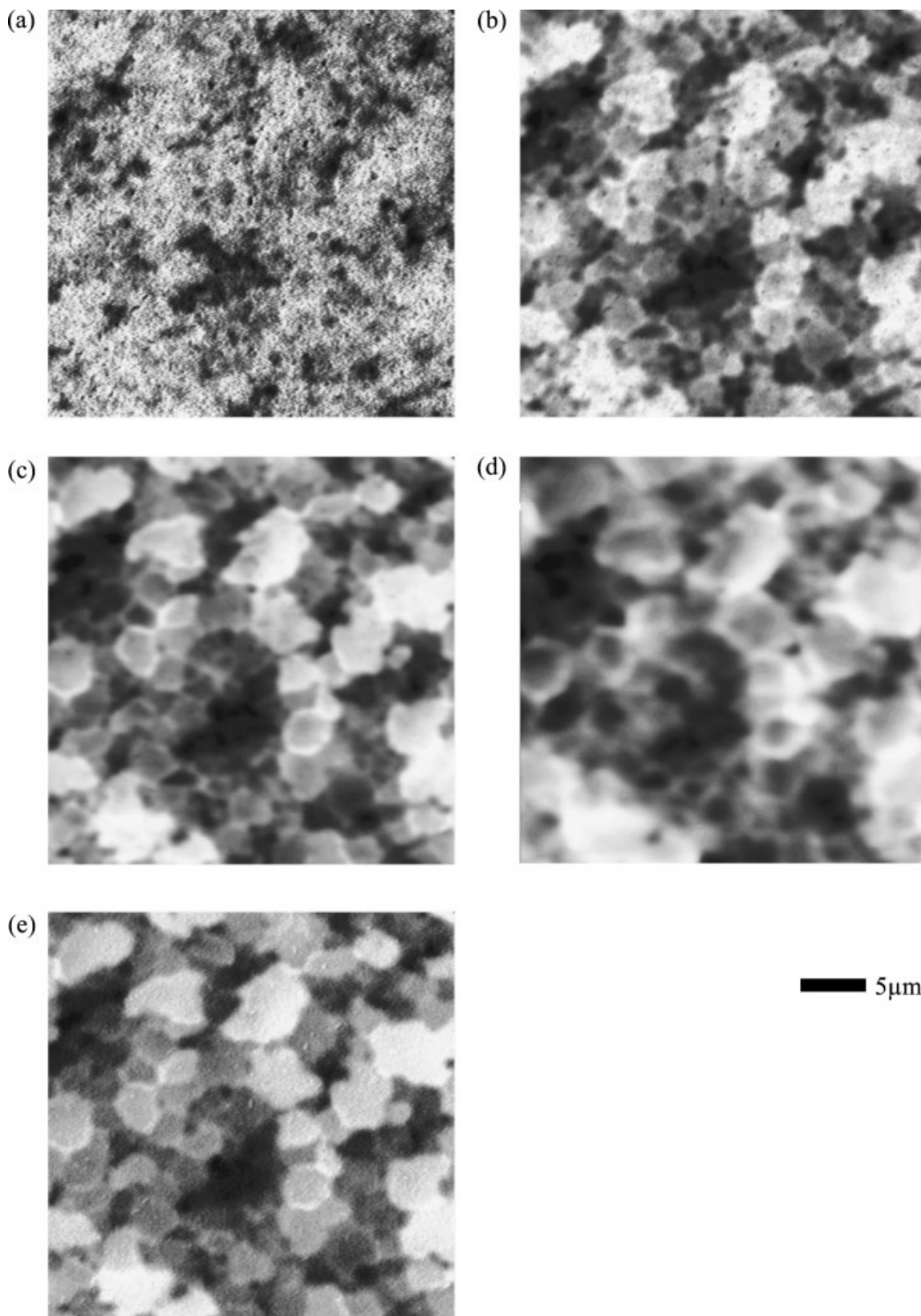
Figure 21. Collection functions for various CdTe/CdS/TCO cells determined by fitting curves of EBIC versus accelerating voltage with the aid of simulated generation functions. Chloride treatment extends the depletion region and increases collection throughout the absorber

Monte Carlo simulation allows the generation function $g(z)$ to be obtained for the multi-layer stack and there is generally no good analytical solution. Fitting can then yield $F(z)$ and although the solutions are not unique it is nevertheless possible to get useful information by choosing appropriate boundary conditions. This is the basis of the measurement of minority-carrier diffusion length from a Schottky diode by Wu and Wittry.¹⁶⁶ Scheer and co-workers have used the method extensively to determine collection functions for chalcopyrite solar cells.^{167,168} Figure 21 gives examples of collection functions obtained from CdTe/CdS/TCO cells from which the glass substrate had been ground and etched off to allow electron beam injection in the optical illumination geometry. In making fits it was assumed that: (a) there was no collection from the CdS (known from spectral response measurements); (b) there is constant collection in the depletion region; and (c) the collection falls off exponentially in the absorber.

Striking differences in the collection function shapes are described in the caption to Figure 21. Given the starting assumptions it is tempting to ascribe the exponential fall-off of the collection function to minority-carrier diffusion. However 'diffusion lengths' extracted from these curves can be up to 4–5 μm while those obtained from other methods are typically $\sim 1 \mu\text{m}$. The high 'effective diffusion lengths' obtained from EBIC in this way might possibly be explained by the concept of sheets of the back-contact material being present at grain boundaries as measured by Levi and co-workers.¹⁶⁹

Both laser and electron beam probes can give injection densities that are many orders of magnitude greater than that of solar irradiation. If the efficiency of carrier collection by a solar cell is measured as a function of injection density, then it is seen to drop sharply from a plateau as the so-called high-injection threshold is surpassed.¹⁷⁰ High injection is defined as the point at which the injected carrier density exceeds the majority carrier density. Usually high injection is avoided in EBIC. Nevertheless, measurement of this threshold at each pixel in a plan-view EBIC image enables a new form of microscopy to be performed that is sensitive to local carrier concentration. Figures 22(a–d) show a series of plan-view EBIC images of a CdTe/CdS/TCO solar cell recorded as a function of beam current. (In all of the micrographs the contrast range is expanded artificially to give a range of 100%.) At low injection (low beam current) the absolute contrast is weak and there is no evidence of grain structure. This is direct evidence of grain boundary passivation. As the beam current is raised

Figure 22. (a–d): EBIC images of a CdTe/CdS solar cell, taken with varying primary beam currents: (a) $1 \times 10^{10} \text{ A}$; (b) $5 \times 10^{10} \text{ A}$; (c) $2 \times 10^9 \text{ A}$; (d) $1 \times 10^8 \text{ A}$; (e) map of current threshold values, constructed using EBIC images (a–d) and further EBIC images taken with different beam currents (not shown). Bright contrast indicates a higher injection threshold and therefore a higher local majority carrier density. All images are to same scale: scale bar, 5 μm



progressively more of each frame enters high injection and the collection is weakened. Grain-to-grain and grain-boundary features are revealed. From a series of such quantitative images recorded with a small beam current interval the high-injection threshold for each pixel was determined. These data were assembled to form an entirely new image, shown in Figure 22(e). There is strong grain-to-grain variation. Importantly, there is often bright contrast at grain boundaries. This indicates local high p -type doping. This would be consistent with an upturn in the conduction band near to grain boundaries, this being the first direct evidence for a mechanism of grain-boundary passivation in this kind of device material.^{165,170} Work on bulk transport in similar films established a more sophisticated model; it is likely that there are resolution issues for the injection-dependent EBIC method.

Overall the EBIC suite of methods constitute a powerful set of tools for investigating critical parameters in thin-film solar cells. However it should be borne in mind that quantitative interpretation of EBIC methods is desirable and that its results should not be taken in isolation.

SMALL-SPOT LIGHT-BEAM-INDUCED CURRENT (LBIC)

Most electrical and optical measurements of solar cells can be described as whole-cell characterization: either the optical source illuminates the entire cell, or it is assumed that the illuminated area represents the cell as a whole. In practice, such measurements are averages, and particularly with thin-film polycrystalline cells, they may mask important local features. The term laser-beam-induced current (LBIC) is commonly applied to measurements made when a laser beam is used to sequentially illuminate localized areas of the cell under study. More generally, optical-beam-induced current refers to selected-area measurements with any light source. There are a number of electron- and optical-beam techniques to probe local regions of a solar cell, but LBIC (or optical-beam-induced current) is the one that probes actual solar cell response.

In 1951, a scanned light spot was first used to determine minority-carrier lifetime from spatial variations in photocurrent.¹⁷¹ By the late 1970s, scanned laser beams were being used to measure photocurrent variations in multicrystalline silicon cells.^{172–174} In the same time frame, the two-dimensional laser scanner, which first used two oscillating mirrors to produce a rastered response map, was developed¹⁷⁵ and was later used to map defects in thin-film solar cells.¹⁷⁶ Various improvements to the two-mirror scanner followed, including reduction of the spot size to 2 μm ¹⁷⁷ and the use of modern computer techniques to capture and store the data.¹⁷⁸ The two-mirror scanner, however, is not well suited to quantitative studies of small areas (dimensions of micrometres), since it is difficult to align and to maintain a highly focused spot when moved over a significant area.

The alternative to moving a laser beam across the cell is to move the cell under the laser beam, either with translation stages¹⁷⁹ or piezoelectric rastering.¹⁸⁰ Modern stepper motors make the translation-stage approach quite straightforward and can reliably position and reposition a solar cell area with uncertainty much less than 1 μm . It is also highly desirable to focus the laser beam to near its diffraction limit and to maintain an intensity similar to the solar intensity that a cell would experience under normal operation. These conditions imply a laser-beam power of the order of 1 nW and photocurrents of the order of 1 nA, clearly requiring lock-in techniques. Such an apparatus has been built, and good-quality photocurrent maps have been reported.^{181–183} Measurements of smaller spatial areas are possible with near-field techniques, but it is difficult to achieve a reasonable signal-to-noise ratio at the solar intensity with currents significantly below 1 nA.

The configuration used at Colorado State University to measure highly localized solar-cell response is shown in Figure 23. The light source is selected from a group of laser diodes of different wavelengths. Finer wavelength control is achieved by varying the laser-diode temperature. Current to the laser is electronically modulated to produce an AC laser beam, and the modulation also provides the reference signal for a lock-in amplifier. Attenuation over a wide dynamic range is set with digital control. The beam is expanded, s -polarization is selected, and the beam is sampled for both intensity impinging on the cell and back-reflection from the cell. Beam steering mirrors allow an accurately parallel and vertical beam to impinge on the objective lens. The objective used (Olympus 1-UB367 SL C Plan Fluoride 40 \times ; 0.55 numerical aperture) is equipped with a correction collar to focus through 0–2.5 mm of glass. It has a working distance of 8.8 mm, which allows ample room for cell contacts. Details of the alignment, focusing and calibration procedures can be found elsewhere.^{181,182}

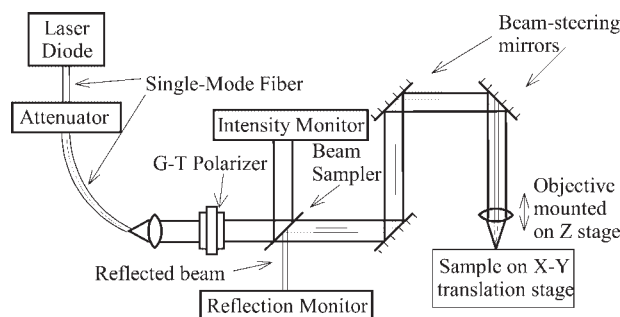


Figure 23. Schematic of small-spot LBIC apparatus used in the analysis of the spatially resolved performance of thin-film solar cells. Taken from Hiltner and Sites¹⁸³

LBIC measurements by the apparatus shown in Figure 23 are made by stepping the cell through the beam in a raster pattern. It takes approximately 20 min to produce a photocurrent map of 101×101 points for a small area, and somewhat longer for larger areas. Generally the first map is taken at low resolution (5×5 mm, $100 \mu\text{m}$ spot), which covers a significant portion of a typical test cell. Then the magnification can then be increased 10 times ($500 \times 500 \mu\text{m}$, $10 \mu\text{m}$ spot) or 100 times ($50 \times 50 \mu\text{m}$, $1 \mu\text{m}$ spot). This process makes it straightforward to zoom in on a small area of particular interest and to return to the same area even after the cell has been removed from the apparatus for other measurements. Photocurrent maps are generally presented as quantum efficiency (QE) at any location. The average QE of such maps generally agrees quite well with QE measured with a conventional system.

Two examples of LBIC studies are presented. The first, shown in Figure 24, is a uniformity comparison between a single-crystal GaAs cell, a good-quality thin-film CdTe cell and a CdTe thin-film cell where a key fabrication step was omitted. The GaAs cell as expected had a very uniform photocurrent response. Its QE is somewhat low, since it did not have an anti-reflection coating. The first CdTe cell, fabricated with the standard CdCl_2 step, has uniformity variations of about 2%. The one fabricated without that step not only has a much-reduced photocurrent response, but also exhibited QE variations of about 20%.

A second example is shown in Figure 25. In this case the left photomap of a typical thin-film CdTe cell was produced with photons (638 nm) well above the CdTe bandgap energy. This area is reexamined seven times as the photon energy is lowered through the band gap. The average QE over this range falls from 80% to about 2%, and there is a clear shift from uniformity to nonuniformity. The explanation in this case is that, during fabrication, sulfur from the CdS window layer diffused into the CdTe absorber. The diffusion is clearly greater in some areas, most probably those corresponding to separations between grains.¹⁸³

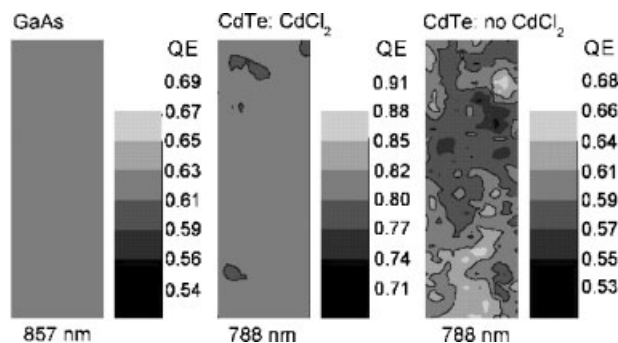


Figure 24. Photocurrent maps of three cells obtained by LBIC. For CdTe/CdS homogeneous performance was achieved only by applying the ubiquitous CdCl_2 treatment. Area shown is $10 \times 10 \mu\text{m}$. Laser spot size is $1 \mu\text{m}$, and intensity is 100 mW/cm^2 . Adapted from Hiltner¹⁸²

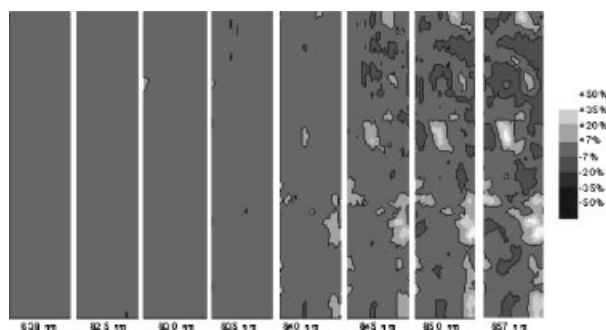


Figure 25. Photocurrent map of a CdTe/CdS cell showing variations with wavelength. Scale is the deviation from average. The nonuniformity in performance at wavelengths is attributed to nonuniform diffusion of S into the CdTe absorber, which has the effect of reducing the bandgap. Area shown is $50 \times 10 \mu\text{m}$. Beam size is $1 \mu\text{m}$, and intensity is 100 mW/cm^2 . Taken from Hiltner and Sites¹⁸³

A number of additional applications of small-spot LBIC measurements on thin-film cells have been reported in recent years, many of which involve variations in cell bias, light intensity or wavelength, spot size or phase of the response signal. One application has been the determination of local internal resistance.^{184,185} Other work, more extensive than in the example shown in Figure 24, has studied the local effects of CdTe post-deposition treatments.^{170,180} Another application is the tracking of changes in CdTe cells, especially the emergence of small dead areas, after they have been exposed to elevated temperatures for extended periods of time.^{181,183,186} Finally, a fertile, but largely unexplored, area for thin-film cells is the extraction of full current/voltage curves at specific localized points on a cell.¹⁸⁷

CONCLUSIONS

Engineering of thin-film PV devices represents a particularly difficult challenge: while in essence the devices are simple, characterization by the methods described in this article reveals the materials to be complex. It is understood that the device performance cannot wholly be described by taking the properties of the component materials in their bulk or simple forms and applying junction theory to them. Instead, either an empirical or a multidisciplinary approach is required. Given that progress in increasing the efficiency of thin-film polycrystalline solar cells has been spasmodic, there is a strong case that work should continue in making links between the materials' properties (in thin-film polycrystalline form) and the properties of the devices made from them. This requires the cooperative effort of many techniques, and of many laboratories.

Acknowledgements

All of the authors would like to express their gratitude to their co-workers and collaborators, without whom this perspective on characterization would not have been formed. JRS is grateful to Dr Jason Hiltner, who built the apparatus shown in Figure 23, and to current students Markus Gloeckler and Timothy Nagle; funding was provided by the US National Renewable Energy Laboratory. CLP, GT, HM, WM, DL and SEA all acknowledge funding from the US Department of Energy under contract DE-AC36-99GO10337.

REFERENCES

1. Yu ET. Nanoscale characterization of semiconductor materials and devices using scanning probe techniques. *Materials Science and Engineering* 1996; **R17**: 147–206.
2. Sacks W. Scanning Probe Microscopy: beyond the Images. In *Les Editions de Physique*, Gauthier S, Joachim C (eds). Les Ulis: France, 1992; 107–163.

3. Binnig G, Rohrer H. Scanning tunneling microscopy. *IBM Journal of Research and Development* 2000; **44**(1–2): 279–293.
4. Chen CJ. *Introduction to Scanning Tunnelling Microscopy*. Oxford University Press: New York, 1993.
5. Binnig G, Quate CF, Gerber CH. Atomic force microscope. *Physical Review Letter* 1986; **56**(9): 930–933.
6. Meyer E. Atomic force microscopy. *Progressing Surface Science* 1992; **41**: 3–49.
7. Sasaki N, Tsukada M. In *Advances in Scanning Probe Microscopy*, Sakurai T, Watanabe Y (eds). Springer: Berlin, 2000; 9–20.
8. Mate CM, McClelland GM, Erlandsson R, Chiang S. Atomic-scale friction of a tungsten tip on a graphite surface. *Physical Review Letter* 1987; **59**(17): 1942–1945.
9. Kalinin SV, Bonnell DA. In *Scanning Probe Microscopy and Spectroscopy, Theory, Techniques, and Applications*, Bonnell D (ed.). Wiley-VCH: New York, 2001; 207–223.
10. Xu Q, Hsu JWP. Electrostatic force microscopy studies of surface defects on GaAs/Ge films. *Journal of Applied Physics* 1999; **85**(5): 2465–2472.
11. Vatel O, Tanimoto M. Kelvin probe force microscopy for potential distribution measurement of semiconductor devices. *Journal of Applied Physics* 1995; **77**(6): 2358–2362.
12. Williams CC. Two-dimensional dopant profiling by scanning capacitance microscopy. *Annual Reviews of Materials Science* 1999; **29**: 471.
13. Marchiando JF, Kopanski JJ. Regression procedure for determining the dopant profile in semiconductors from scanning capacitance microscopy data. *Journal of Applied Physics* 2002; **92**(10): 5798–5809.
14. McMahon WE, Olson JM. Atomic-resolution STM study of a structural phase transition of steps on vicinal As/Ge(100). *Physical Review B* 1999; **60**(23): 15999–16005.
15. Sadewasser S, Glatzel Th, Rusu M, Jager-Waldau A, Lux-Steiner MCh. High-resolution work function imaging of single grains of semiconductor surfaces. *Applied Physics Letters* 2002; **80**(16): 2979–2981.
16. Glatzel Th, Marron DF, Schedel-Niedrig Th, Sadewasser S, Lux-Steiner MCh. CuGaSe₂ solar cell cross section studied by Kelvin probe force microscopy in ultrahigh vacuum. *Applied Physics Letters* 2002; **81**(11): 2017–2019.
17. Jiang C-S, Moutinho HR, Geisz JF, Friedman DJ, Al-Jassim MM. Direct measurement of electrical potentials in GaInP₂ solar cells. *Applied Physics Letters* 2002; **81**(14): 2569–2571.
18. Visoly-Fisher I, Cohen SR, Cahen D. Direct evidence for grain-boundary depletion in polycrystalline CdTe from nanoscale-resolved measurements. *Applied Physics Letters* 2003; **82**(4): 556–558.
19. Rezek B, Stuchlik J, Fejfar A, Kocka J. Microcrystalline silicon thin films studied by atomic force microscopy with electrical current detection. *Journal of Applied Physics* 2002; **92**(1): 587–593.
20. Moutinho HR, Al-Jassim MM, Levi DH, Dippo PC, Kazmerski LL. Effects of CdCl₂ treatment on the recrystallization and electro-optical properties of CdTe thin films. *Journal of Vacuum Science and Technology A* 1998; **16**(3): 1251–1257.
21. Moutinho HR, Dhere RG, Al-Jassim MM, Levi DH, Kazmerski LL. Investigation of induced recrystallization and stress in close-spaced sublimated and radio-frequency magnetron sputtered CdTe thin films. *Journal of Vacuum Science and Technology A* 1999; **17**(4): 1793–1798.
22. Moutinho HR, Dhere RG, Ballif C, Al-Jassim MM, Kazmerski LL. Alternative procedure for the fabrication of close-spaced sublimated CdTe solar cells. *Journal of Vacuum Science and Technology A* 2000; **18**(4): 1599–1603.
23. Moutinho HR, Albin D, Yan Y, Dhere RG, Li X, Perkins C, Jiang C-S, To B, Al-Jassim MM. Deposition and properties of CBD and CSS thin films for solar cell application. *Thin Solid Films* 2003; **436**: 175–180.
24. Brentano JCM. *Journal of Applied Physics* 1946; **17**: 420.
25. Seeman H. *Annalen der Physik* 1919; **59**: 445.
26. Bohlin H. *Annalen der Physik* 1920; **61**: 421.
27. Klug HP, Alexander LE. *X-Ray Diffraction Procedures for Polycrystalline and Amorphous Materials*. Wiley: New York, 1974; 290–310.
28. James RW. *The Optical Principles of the Diffraction of X-Rays*. Oxbow Press: Woodbridge, CT, 1982.
29. Gilles B. *Thin Film Characterisation by Advanced X-ray Diffraction Techniques*, Cappuccio G, Terranova ML (eds). Laboratori Nazionali Di Frascati: Frascati, Italy, 1996; 177.
30. Harris GB. *Philosophical Magazine* 1952; **43**: 113.
31. Nelson JB, Riley DP. *Proceedings of the Physical Society* 1945; **57**: 160.
32. Taylor A, Sinclair H. *Proceedings of the Physical Society* 1945; **57**: 126.
33. Warren BE. *X-Ray Diffraction*. Dover: New York, 1990; 253.
34. Szanto IS, Varga L. *Journal of Applied Crystallography* 1969; **2**: 72.

35. Young RA, Wiles DB. Profile shape functions in rietveld refinements. *Journal of Applied Crystallography* 1982; **15**: 430–438.
36. Toraya H. Whole-powder-pattern fitting without reference to a structural model—application to X-ray-powder diffractometer data. *Journal of Applied Crystallography* 1986; **19**: 440–447.
37. Cullity BD. *Elements of X-Ray Diffraction*. Addison-Wesley: Reading, MA, 1956; 191.
38. Rietveld HM. *Journal of Applied Crystallography* 1969; **2**: 65.
39. Battiston GA, Gerbasi R. *Thin Film Characterisation by Advanced X-ray Diffraction Techniques*, Cappuccio G, Terranova ML (eds). Laboratori Nazionali di Frascati: Frascati, Italy, 1996; 225.
40. Ma C-H, Huang J-H, Chen H. Residual stress measurement in textured thin film by grazing-incidence X-ray diffraction. *Thin Solid Films* 2002; **418**: 73–78.
41. Segmuller A, Murakami M. *Treatise on Materials Science and Technology*, Vol. 27. Academic: New York, 1988; 143.
42. van Leeuwen M, Kamminga J-D, Mittemeijer EJ. Diffraction stress analysis of thin films: modeling and experimental evaluation of elastic constants and grain interaction. *Journal of Applied Physics* 1999; **86**(4): 1904–1914.
43. McCandless BE. *Symp. Rec. MRS* 2001; **668**: H1-6-1.
44. McCandless BE, Engelmann MG, Birkmire RW. Interdiffusion of CdS/CdTe thin films: modeling X-ray diffraction line profiles. *Journal of Applied Physics* 2001; **89**(2): 988–994.
45. Engelmann M, McCandless BE, Birkmire RW. Formation and analysis of graded CuIn(S_{1-y}S_y)(2) films. *Thin Solid Films* 2001; **387**: 14–17.
46. Brewster D. *Treatise on Optics*. Longman, Rees, Orme, Brown, Green and Taylor: London, 1831; 108.
47. Drude P. *Annalen der Physikalische Chemie* 1889; **36**: 532.
48. Rothen A. *Review of Scientific Instruments* 1945; **16**: 26.
49. Bruggeman DAG. *Annals of Physics* (Leipzig) 1935; **24**: 636.
50. Paulson PD, Birkmire RW, Shafarman WN. TI Optical characterization of CuIn_{1-x}Ga_xSe₂ alloy thin films by spectroscopic ellipsometry. *Journal of Applied Physics* 2003; **94**: 879–888.
51. Wei K, Pollak FH, Freeouf JL, Shvydka D, Compaan AD. Optical properties of CdTe_{1-x}S_x (0 ≤ x ≤ 1): experiment and modeling. *Journal of Applied Physics* 1999; **85**: 7418–7425.
52. Hermann AM, Gonzalez C, Ramakrishnan PA, Balzar D, Popa N, Rice P, Marshall CH, Hilfiker JN, Tiwald T, Sebastian PJ, Calixto ME, Bhattacharya RN. Fundamental studies on large area Cu(In,Ga)Se₂ films for high efficiency solar cells. *Solar Energy Materials and Solar Cells* 2001; **70**: 345–361.
53. Snyder PG, Woollam JA, Alterovitz SA, Johs B. Modeling ALXGA1-XAS optical-constants as functions of composition. *Journal of Applied Physics* 1990; **68**: 5925–5926.
54. Tiwald TE, Thompson DW, Woollam JA, Pepper SV. Application of IR variable angle spectroscopic ellipsometry to the determination of free carrier concentration depth profiles. *Thin Solid Films* 1998; **313**: 661–666.
55. Paulson PD. *Study of Deposition and Post Deposition Treatments on CdS/CdTe Thin Film Solar Cells*, PhD Thesis. Indian Institute of Technology, Delhi, 1997.
56. Xiong Y-M, Wong CC, Saitoh T. *Proceedings of the 1st WCPEC*, Hawaii, 5–9 December, 1994; 1759.
57. Ferlauto AS, Ferreira GM, Koval RJ, Pearce JM, Wronski CR, Collins RW, Al-Jassim MM, Jones KM. *Proceedings of the 29th PVSC*, New Orleans, 2002; 1076.
58. Fujiwara H, Koh J, Lee Y, Wronski CR, Collins RW. *Proceedings of the 26th PVSC*, Anaheim, CA, 30 September, 3 October, 1997; 599.
59. Tu KN, Rosenberg R. *Analytical Techniques for Thin-Film Analysis*. Academic: San Diego, 1988.
60. Williams DB, Carter CB. *Transmission Electron Microscopy: A Textbook for Materials Science*. Plenum: New York, 1996.
61. Reimer L. *Transmission Electron Microscopy, Physics of Image Formation and Microanalysis*, 3rd edn. Springer: New York, 1993.
62. Williams DB. *Practical Analytical Electron Microscopy in Material Science*, 2nd edn. Philips Electron Optics Publishing Group: Mahwah, NJ, 1987.
63. Spence JCH. *Experimental High-Resolution Electron Microscopy*. Oxford University Press: Oxford, 1988.
64. Cherns D. *High-Resolution Transmission Microscopy of Surfaces and Interfaces in Analytical Techniques for Thin-Film Analysis*, Tu KN, Rosenberg R (eds). Academic: San Diego, 1988; 297–335.
65. Cousins MA, Durose K. Near-interface TEM of CdTe in CdTe/CdS solar cells. *Proceedings of the 16th European Photovoltaic Solar Energy Conference and Exhibition*, Scheer H, McNelis B, Pals W, Ossenbrink H, Helm P (eds). James: London, 2000; 835–838.
66. Anderson RM (ed.). Specimen preparation for transmission electron microscopy of materials I. *Materials Research Society Symposium Proceedings*, Vol. 155. MRS: Pittsburgh, PA, 1989.

67. Anderson RM, Tracy B, Bravman J (eds). Specimen preparation for transmission electron microscopy of materials II. *Materials Research Society Symposium Proceedings*, Vol. 199. MRS: Pittsburgh, PA, 1990.
68. Anderson RM, Tracy B, Bravman J (eds). Specimen preparation for transmission electron microscopy of materials III. *Materials Research Society Symposium Proceedings*, Vol. 254. MRS: Pittsburgh, PA, 1992.
69. Al-Jassim MM, Dhere RG, Jones KM, Hassoon FS, Sheldon P. *Proceedings of the 2nd World Conference of Photovoltaic Solar Energy Conversion*, Vol. 1, Vienna, 6–10 July 1998; 1063.
70. Nadenau V, Hariskos D, Schock H-W, Krejci M, Haug F-J, Tiwari AN, Zogg H, Kistorz G. Microstructural study of the CdS/CuGaSe₂ interfacial region in CuGaSe₂ thin film solar cells. *Journal of Applied Physics* 1999; **85**: 534–542.
71. Terheggen M, Heinrich H, Kistorz G, Baetzner D, Romeo A, Tiwari AN. Analysis of bulk and interface phenomena in CdTe/CdS thin-film solar cells. *Interface Science* 2003; in the press.
72. Romeo A, Bätzner DL, Zogg H, Tiwari AN. Recrystallization in CdTe/CdS. *Thin Solid Films* 2000; **361–362**: 420–425.
73. Terheggen M, Heinrich H, Kistorz G, Romeo A, Baetzner D, Tiwari AN, Bosio A, Romeo N. Structural and chemical interface characterization of CdTe solar cells by transmission electron microscopy. *Thin Solid Films* 2003; **431**: 262–266.
74. Pennycook SJ. *Handbook of Microscopy*, Vol. 2, VanDyck D, Van Landuyt J, Van Tendeloo G (eds). VCH: Weinheim, 1997.
75. Briggs D, Seah MP. *Practical Surface Analysis: Auger and X-ray Photoelectron Spectroscopy*, Vol. 1, 2nd edn. Wiley: Chichester, 1994.
76. Mróz S. Physical foundation of quantitative Auger analysis. *Progress in Surface Science* 1994; **46**(4): 377–437.
77. Czanderna AW, Madey TE, Powell CJ. *Beam Effects, Surface Topography, and Depth Profiling in Surface Analysis*. Plenum: New York, 1998.
78. Seah MP, Spencer SJ. AES of bulk insulators—control and characterization of the surface charge. *Journal of Electron Spectroscopy and Related Phenomena* 2000; **109**: 291–308.
79. King PL. Artifacts in AES microanalysis for semiconductor analysis. *Surface and Interface Analysis* 2000; **30**: 377–382.
80. Bohne W, Fenske F, Kelling S, Schöpke A, Selle B. Refined RBS and AES techniques for the analysis of thin films used in photovoltaic devices. *Physica Status Solidi B* 1996; **194**(1): 69–78.
81. Kowalski BJ, Orłowski BA, Ghijsen J. XPS study of CdTe(110) surface oxidation process. *Surface Science* 1998; **413**: 544–554.
82. Debiemme-Chouvy C, Marín FI, Roll U, Bujor A, Etcheberry M. Detection of cadmium oxides on a CdTe substrate by X-AES. *Surface Science* 1996; **352–354**: 495–498.
83. Henrich VE, Cox PA. *The Surface Science of Metal Oxides*. Cambridge University Press: Cambridge, 1994.
84. Harju R, Karpov VG, Grecu D, Dorer G. Electron-beam induced degradation in CdTe photovoltaics. *Journal of Applied Physics* 2000; **88**(4): 1794–1801.
85. Hofmann S. Ultimate depth resolution and profile reconstruction in sputter profiling with AES and SIMS. *Surface and Interface Analysis* 2000; **30**: 228–236.
86. Zalar A. Sample rotating in Auger electron spectroscopy depth profiling. *Journal of Vacuum Science and Technology A* 1987; **5**(5): 2979–2980.
87. Brühwiler PA, Karis O, Mårtensson N. Charge-transfer dynamics studied using resonant core spectroscopies. *Review of Modern Physics* 2002; **74**(3): 703–740.
88. Weightman P. Auger spectroscopy and the electronic structure of semiconductors. *Journal of Electron Spectroscopy and Related Phenomena* 1998; **93**(1–3): 165–174.
89. Chambers SA, Tran TT, Hileman TA. Auger electron spectroscopy as a real-time compositional probe in molecular beam epitaxy. *Journal of Vacuum Science and Technology A* 1995; **13**(1): 83–91.
90. Chambers SA. Elastic scattering and interference of backscattered primary, Auger and X-ray photoelectrons at high kinetic energy: principles and applications. *Surface Science Reports* 1992; **16**(6): 263.
91. Idzerda YU. Role of emission character in Auger electron diffraction. *Surface Review and Letters* 1997; **4**(1): 161–177.
92. Wilson RG, Stevie FA, Magee CW. *Secondary Ion Mass Spectrometry: A Practical Handbook for Depth Profiling and Bulk Impurity Analysis*. Wiley-Interscience: New York, 1989.
93. Benninghoven A, Rudenauer FG, Werner HW. *Secondary Ion Mass Spectrometry: Basic Concepts, Instrumental Aspects, Applications and Trends*. Wiley-Interscience: New York, 1987.
94. The entire series of proceedings from the biennial international SIMS conferences, SIMS II–SIMS XIII. Various publishers, 1979–2003.

95. Vickerman JC (ed.). *Surface Analysis—The Principal Techniques*. Wiley: New York, 1997.
96. Feldman LC, Mayer JW. *Fundamentals of Surface and Thin Film Analysis*. Prentice Hall: London, 1986.
97. Branz HM, Asher S, Gleskova H, Wagner S. Light-induced D diffusion measurements in hydrogenated amorphous silicon: testing H metastability models. *Physical Review B* 1999; **59**: 5513–5520.
98. Jackson WB, Santos PV, Tsai CC. Role of clustering in hydrogen transport in silicon. *Physical Review B* 1993; **47**: 9993–9996.
99. Chou HC, Rohatgi A, Jokerst NM, Thomas EW, Kamra S. Copper migration in CdTe heterojunction solar cells. *Journal of Electronic Materials* 1996; **25**: 1093–1098.
100. Dobson KD, Visoly-Fisher I, Hodes G, Cahen D. Stability of CdTe/CdS thin-film solar cells. *Solar Energy Materials and Solar Cells* 2000; **62**: 295–325.
101. Asher SE, Hasoon FS, Gessert TA, Young MR, Sheldon P, Hiltner J, Sites J. Determination of Cu in CdTe/CdS devices before and after accelerated stress testing. *Proceedings of the 28th IEEE Photovoltaic Specialists Conference*, Anchorage, 2000; 479–482.
102. Gessert TA, Duda D, Asher SE, Narayansamy C, Rose D. Effects of Cu from ZnTe: Cu contacts in CdS/CdTe cells. *Proceedings of the 28th Photovoltaic Specialists Conference*, Anchorage, 2000; 654–657.
103. Durose K, Cousins MA, Boyle DS, Beier J, Bonnet D. Grain boundaries and impurities in CdTe/CdS solar cells. *Thin Solid Films* 2002; **403–404**: 396–404.
104. Rose DR, Hasoon FS, Dhere RG, Albin DS, Ribelin RM, Li XS, Mahathongdy Y, Gessert TA, Sheldon P. Fabrication procedures and process sensitivities for CdS/CdTe solar cells. *Progress in Photovoltaics: Research Applications* 1999; **7**: 331–340.
105. Asher SE, Reedy Jr RC, Dhere R, Gessert TA, Young MR. *Program and Proceedings: NCPV Program Review Meeting 2000*, 16–19 April 2000, Denver, CO; *NICH Report BK-520-28064*, 2000; 275–276.
106. Gnaser H. Improved quantification in secondary-ion mass-spectrometry detecting MCs⁺ molecular-ions. *Journal of Vacuum Science and Technology A* 1994; **12**: 452–456.
107. Gabor A, Tuttle JR, Albin DS, Contreras MA, Noufi R. High-efficiency CUINXGA1-XSE2 solar-cells made from (INX,GA1-X)2SE3 precursor films. *Applied Physics Letters* 1994; **65**: 198–200.
108. Mönch W. *Semiconductor Surfaces and Interfaces*. Springer: Heidelberg, 1993.
109. Fahrenbruch AL, Bube RH. *Fundamentals of Solar Cells*. Academic: New York, 1983.
110. Hüfner S. *Photoelectron Spectroscopy, Springer Series in Solid State Sciences*. Springer: Berlin, 1995.
111. Cardona M, Ley L (eds). *Photoemission in Solids I&II, Topics in Applied Physics*. Springer: Berlin, 1978, 1979.
112. Koningsberger DC, Prins R (eds). *X-ray Absorption—Principles, Applications, Techniques of EXAFS, SEXAFS, XANES*. Wiley: New York, 1988.
113. See articles in *Journal of Electron Spectroscopy and Related Phenomena* 2000; **110/111**.
114. Ade H (ed.). Spectromicroscopy. *Journal of Electron Spectroscopy and Related Phenomena* 1997; **84**.
115. Horn K, Alonso M, Cimino R. Non-equilibrium effects in photoemission from metal-semiconductor interfaces. *Applied Surface Science* 1992; **56–58**: 271–289.
116. Schlaf R, Klein A, Pettenkofer C, Jaegermann W. Laterally inhomogeneous surface potential distribution and photovoltage at clustered In/WSe₂ (0001) interfaces. *Physical Review B* 1993; **48**: 14242.
117. Capasso F, Margaritondo G (eds). *Heterojunction Band Discontinuities*. North-Holland: Amsterdam, 1987.
118. Fritzsche J, Schulmeyer T, Thißen A, Klein A, Jaegermann W. Interface modification of CdTe thin film solar cells by CdCl₂-activation. *Thin Solid Films* 2003; **431–432**: 267.
119. Schulmeyer T, Fritzsche J, Thißen A, Klein A, Jaegermann W, Campo M, Beier J. Effect of *in situ* UHV CdCl₂ activation on the electronic properties of CdTe thin film solar cells. *Thin Solid Films* 2003; **431**: 84–89.
120. Fritzsche J, Gunst S, Thissen A, Gegenwart R, Klein A, Jaegermann W. CdTe thin film solar cell: the SnO₂/CdS front contact. *Materials Research Society Symposium Proceedings* 2001; **668**: H5-1.
121. Niles DW, Höchst H. Band offsets and interfacial properties of cubic CdS grown by molecular-beam epitaxy on CdTe(110). *Physical Review B* 1990; **41**: 12710.
122. Klein A, Fritzsche J, Jaegermann W, Schön JH, Kloc Ch, Bucher E. Fermi level dependent defect formation at CuInSe₂ interfaces. *Applied Surface Science* 2000; **166**: 508.
123. Klein A, Jaegermann W. Fermi level dependent defect formation in Cu-chalcopyrite semiconductors. *Applied Physics Letters* 1999; **74**: 2283.
124. Schulmeyer T, Hunger R, Jaegermann W, Klein A, Kniese R, Powalla M. Interface formation between polycrystalline Cu(InGa)Se- and II–VI compounds. *Proceedings of the 3rd World Conference on Photovoltaic Energy Conversion*, Osaka, 2003;

125. Schulmeyer T, Hunger R, Lebedev M, Klein A, Jaegermann W, Kniese R, Powalla M. Submitted to *Applied Physics Letters* 2003.
126. Heske C, Groh U, Fuchs O, Umbach E, Franco N, Bostedt C, Terminello LJ, Perera RCC, Hallmeier KH, Preobrajenski A, Szargan R, Zweigart S, Riedl W, Karg F. X-Ray emission spectroscopy of Cu(In,Ga)(S,Se)₂-based thin film solar cells: electronic structure, surface oxidation, and buried interfaces. *Physica Status Solidi A* 2001; **187**: 13.
127. Weinhardt L, Gleim T, Fuchs O, Heske C, Umbach E, Bär M, Muffler H-J, Fischer C-H, Lux-Steiner MC, Zubavichus Y, Niesen TP, Karg F. CdS and Cd(OH)₂ formation during Cd treatments of Cu(In,Ga)(S,Se)₂ thin-film solar cell absorbers. *Applied Physics Letters* 2003; **82**: 571.
128. Morkel M, Weinhardt L, Lohmüller B, Heske C, Umbach E, Riedl W, Zweigart S, Karg F. Flat conduction-band alignment at the CdS/CuInSe₂ thin-film solar-cell heterojunction. *Applied Physics Letters* 2001; **79**: 4482.
129. Hunger R, Lebedev M, Schulmeyer Th, Klein A, Jaegermann W, Sakurai K, Niki S, Kniese R, Powalla M. Removal of surface inversion of CuInSe₂ by NH₃ etching. *Proceedings of the 3rd World Conference on Photovoltaic Energy Conversion*, Osaka, 2003;
130. Kraft D, Thissen A, Campo M, Beerbom M, Mayer T, Klein A, Jaegermann W. Electronic properties of chemically etched CdTe thin films: role of Te for back contact formation. *Materials Research Society Symposium Proceedings* 2001; **668**: H7.
131. Liu G, Jaegermann W, He J, Sundström V. Characterisation of the TiO₂/ZnPcGly heterointerface: alignment of energy levels. *Journal of Physical Chemistry B* 2002; **106**: 5814.
132. Tiefenbacher S, Pettenkofer C, Jaegermann W. Preparation and characterisation of TiO₂/CdTe interfaces—electrical properties and the implications for solar cells. *Journal of Applied Physics* 2002; **91**: 1984.
133. Shroder DK. *Semiconductor Material and Device Characterization*. Wiley: New York, 1990; 490–494.
134. Cardenas M, Mendoza-Alvarez JG, Sanchez-Sinencio F, Zelaya O, Menezes C. Photoluminescent properties of films of CdTe on glass grown by a hot-wall-close space vapor transport method. *Journal of Applied Physics* 1984; **56**(10): 2977–2980.
135. Dean PJ, Herbert DC. *Bound Excitons in Semiconductors*, Cho K, (ed.). Springer: Berlin, 1979.
136. Dean PJ. In *Progress in Solid State Chemistry*, Vol. 8, McCaldin JO, Somarjai G (eds). Pergamon: Oxford, 1973.
137. Miller RC, Bhat R. Some remarks on excitation spectra versus photoluminescence spectra for the evaluation of quantum wells. *Journal of Applied Physics* 1988; **64**(7): 3647–3649.
138. Pankove JJ. *Optical Processes in Semiconductors*. Dover: New York, 1971; 107–159.
139. Yu P, Cardona M. *Fundamental of Semiconductors*, 2nd edn. Springer: Berlin, 1999; 333–361.
140. Gilliland GD. Photoluminescence spectroscopy of crystalline semiconductors. *Materials Science and Engineering Reports* 1997; **18**: 99–354.
141. Keyes B, Dippo P, Metzger W, AbuShama J, Noufi R. Cu(In,Ga)Se₂ thin-film evolution during growth—a photoluminescence study. *Proceedings of the 29th IEEE PVSC*, New Orleans, 2002; 511–514.
142. Zanio K. *Semiconductors and Semimetals*, Vol. 13, Willardson RK, Beer AC (eds). Academic: New York, 1978; 90–161.
143. Dirnstorfer I, Burkhardt W, Kriegerseis W, Osterreicher I, Alves H, Hofmann D, Ka O, Polity A, Meyer B, Braunger D. Annealing studies on CuIn(Ga)Se₂: the influence of gallium. *Thin Solid Films* 2000; **361**(1): 400–405.
144. Street RA. *Hydrogenated Amorphous Silicon*, chapters 4, 6–8. Cambridge University Press: Cambridge, 1991.
145. Yue G, Han D, Williamson D, Yang J, Lord K, Guha S. Electronic states of intrinsic layers in n-i-p solar cells near amorphous to microcrystalline transition studied by photoluminescence spectroscopy. *Applied Physics Letters* 2000; **77**(20): 3185–3187.
146. O'Connor DV, Phillips D. *Time-correlated Single Photon Counting*. Academic: San Diego, 1984.
147. Landsberg PT. *Recombination in Semiconductors*. Cambridge University Press: New York, 1991.
148. Ahrenkiel RK. *Semiconductors and Semimetals, Minority Carriers in III–V Semiconductors: Physics and Applications*, Vol. 39, Willardson RK, Beer AC (eds). Academic: New York, 1978; 148.
149. Metzger WK, Albin D, Levi D, Sheldon P, Li X, Keyes BM, Ahrenkiel RK. Correlations of photoluminescence decay lifetime, CdCl₂ treatment, and microstructure with CdTe solar cell performance. *Journal of Applied Physics* 2003; **94**(5): 3549.
150. Dhere RD. *Study of the CdS/CdTe Interface and its Relevance to Solar Cell Properties*. PhD Thesis, University of Colorado at Boulder, 1997.
151. Sheng SL, Stanbery BJ, Huang CH, Chang CH, Chang YS, Anderson TJ. Effects of buffer layer processing on CIGS excess carrier lifetime: application of dual-beam optical modulation to process analysis. *Proceedings of the 25th IEEE Photovoltaic Specialists Conference*, Washington DC, 1996; 821–824.

152. Huang CH, Sheng SL, Stanbery BJ, Chang CH, Anderson TJ. Investigation of buffer layer process on CIGS solar cells by dual beam optical modulation technique. *Proceedings of the 26th IEEE Photovoltaic Specialists Conference*, Anaheim, CA, 1997; 407–410.
153. Ohnesorge B, Weigand R, Bacher G, Forchel A, Riedl W, Karg FH. Minority-carrier lifetime and efficiency of Cu(In,Ga)Se₂ solar cells. *Applied Physics Letters* 1998; **73**(9): 1224–1226.
154. Probst V, Stetter W, Riedl W, Vogt H, Wendl M, Calwer H, Zweigart S, Ufert KD, Freienstein B, Cerva H, Karg FH. Rapid CIS-process for high efficiency PV-modules: development towards large area processing. *Thin Solid Films* 2001; **387**: 262–267.
155. Joy DC. *Monte Carlo Modelling for Electron Microscopy and Microanalysis*. Oxford University Press: New York, 1995.
156. Leamy HJ. Charge collection scanning electron microscopy. *Journal of Applied Physics* 1982; **53**(6): R51.
157. Holt DB, Joy DC. *SEM Micro-characterisation of Semiconductors, Techniques of Physics Series*, Vol. 12, March NH (ed.). Academic: London, 1989.
158. Ehrenberg W, Gibbons DJ. *Electron Bombardment Induced Conductivity and Its Applications*. Academic: London, 1981.
159. Russell GJ, Robertson MJ, Vincent B, Woods J. An electron beam induced current study of grain boundaries in zinc selenide. *Journal of Materials Science* 1980; **15**: 939–944.
160. Holt DB, Raza B, Wojcik A. EBIC studies of grain boundaries. *Materials Science and Engineering* 1996; **B42**: 14–23.
161. Russell JD, Leach C. Problems associated with imaging resistive barriers in BaTiO₃ PTC ceramics using the SEM conductive mode. *Journal of the European Ceramic Society* 1995; **15**: 617–622.
162. Durose K, Sadler JRE, Yates AJW, Szczerbakow A. PR-EBIC study of the electrical activity of grain boundaries in CdTe and Cd(S,Te). *Proceedings of the 28th IEEE Photovoltaic Specialists Conference*, Anchorage, 2000; 487.
163. Kenny RH, McClure JC. Electron beam induced currents in thin-film CdS-CdTe heterojunction cells. *Proceedings of the 8th European Conference on Solar Energy Conversion*, Vol. 2, Florence, 9–13 May, 1988; 1097.
164. Rechid J, Kampmann A, Reineke-Koch R. Characterising superstrate CIS solar cells with electron beam induced current. *Thin Solid Films* 2000; **361–362**: 198–202.
165. Edwards PR, Galloway SA, Durose K. EBIC and luminescence mapping of CdTe/CdS solar cells [Publisher's erratum: *Thin Solid Films* 2000; **361–362**: 364–370]. *Thin Solid Films* 2000; **372**: 284–291.
166. Wu CJ, Wittry DB. Investigation of minority-carrier diffusion lengths by electron bombardment of Schottky barriers. *Journal of Applied Physics* 1978; **45**(9): 2827.
167. Scheer R, Knieper C, Stolt L. Depth dependent collection functions in thin film chalcopyrite solar cells. *Applied Physics Letters* 1995; **67**(20): 3007.
168. Scheer R, Wilhelm M, Nadenau C, Schock HW, Stolt L. Collection functions in chalcopyrite heterojunction solar cells: a comparison of Cd(In,Ga)(Se,S)₂ absorbers. *Proceedings of the 14th European PVSEC*, Barcelona, 1997;
169. Levi DH, Woods LM, Albin DS, Gessert TA, Niles DW, Swartzlander A, Rose DH, Ahrenkiel RK, Sheldon P. *Proceedings of the 26th IEEE Photovoltaic Specialists Conference*, Anaheim, 1997; 351–354.
170. Galloway SA, Edwards PR, Durose K. Characterisation of thin-film CdS/CdTe solar cells using electron beam induced current. *Solar Energy Materials and Solar Cells* 1999; **57**: 61–74.
171. Goucher FS, Pearson GL, Sparks M, Teal GK, Shockley W. Theory and experiment for a germanium *p-n* junction. *Physical Review* 1951; **81**: 637.
172. Zook JD. Effects of grain boundaries in polycrystalline solar cells. *Applied Physics Letters* 1980; **37**: 223–226.
173. Hari Rao CV, Bates HE, Ravi KV. Electrical effects of SiC inclusions in EFG silicon ribbon solar cells. *Journal of Applied Physics* 1976; **47**: 2614.
174. Belouet C, Hervo J, Matres R, Phuoc NT, Pertus M. Growth and characterization of polysilicon layers achieved by the ribbon-against-drop (RAD) process. *Proceedings of the 13th IEEE Photovoltaics Specialists Conference* 1978; 131–136.
175. Lile D, Davis N. *Method and Apparatus for Semiconductor Profiling Using an Optical Probe*. US Patent 4,0051,437 (September 27, 1977).
176. Phillips JE, Birkmire RW, Lasswell PG. Stability of thin-film Cu₂S-based solar cells at *V_{OC}* under continuous illumination. *Proceedings of the 16th IEEE Photovoltaics Specialists Conference* 1982; 719–722.
177. Damaskinos S. An improved laser scanning technique for evaluation of solar cells: application to CuInSe₂/(CdZn)S devices. *Solar Cells* 1989; **23**: 151.
178. Matson RJ, Emery KA, Eisgruber IL, Kazmerski LL. The large-scale laser scanner: milli-characterization of photovoltaic cells and modules. *Proceedings of the 12th European PVSEC* 1994; 1222–1225.

179. Sawyer WD. An improved method of light-beam-induced current characterization of grain boundaries. *Journal of Applied Physics* 1986; **59**: 2361.
180. Galloway SA, Brinkman AW, Durose K, Wilshaw PR, Holland AJ. A study of the effects of post deposition treatment on CdS/CdTe thin film solar cells using high resolution OBIC. *Applied Physics Letters* 1996; **68**: 3725–3727.
181. Hiltner JF, Sites JR. High-resolution laser stepping measurements on polycrystalline solar cells. *Proceedings of the 16th European PVSEC* 2000; 630–633.
182. Hiltner JF. *Investigation of Spatial Variations in Collection Efficiency of Solar Cells*. PhD Thesis, Colorado State University, 2001. <http://www.physics.colostate.edu/groups/photovoltaic/PDFs/JHThesis.pdf>.
183. Hiltner JF, Sites JR. Micron-resolution photocurrent of CdTe solar cells using multiple wavelengths. *Proceedings of the Materials Research Society* 2001; **668**: H9-8-1–H9-8-6.
184. Delahoy AE, Payne AM. Determination of the internal series resistance of CIS and CIGS photovoltaic cell structures. *Proceedings of the 25th IEEE Photovoltaics Specialists Conference* 1996; 841–844.
185. McMahon TJ, von Rodern B. Effect of light intensity of current collection in thin-film solar cells. *Proceedings of the 26th IEEE Photovoltaic Specialists Conference* 1997; 377–380.
186. Pudov AO, Gloeckler M, Demtsu SH, Sites JR, Barth KL, Enzenroth RA, Sampath WS. Effect of back-contact copper concentration on CdTe cell operation. *Proceedings of the 29th IEEE Photovoltaic Specialists Conference* 2002; 760–763.
187. Carstensen J, Popkirov G, Bahr J, Föll H. Cello: an advanced LBIC measurement for solar cell local characterization. *Proceedings of the 16th European PVSEC* 2001; 1627–1630.